Modeling and Energy Balancing Control of Modular Multilevel Converters Using Perturbation Theory for Quasi-Periodic Systems

Albrecht Gensior and Hendrik Fehr

***Abstract*—The most common modular multilevel converter (MMC) balancing solution uses the circulating current to generate additional powers in conjunction with the terminal voltages including the common-mode voltage, relying on distinct frequencies. Usually, the energies affected by each frequency component are identified assuming constant amplitudes, which neglects the inevitable impact on the other energies that inherently arises from the amplitude variation caused by the feedback. Two issues have received insufficient attention: 1) the approach does not provide a dynamic model of the converter variables suitable for model-based balancing control design, and 2) studies are missing that explore the limitations caused by the usually neglected mutual interactions of the energies. Thus, an MMC model is derived using perturbation theory for quasi-periodic systems that lends itself to balancing control design, as it solely describes the average of the energies. Moreover, the impact of the mutual interactions is evaluated, revealing the characteristics of a tradeoff between model accuracy and balancing speed, that is inherent to any similar scheme. Further contributions are the calculation of the energy ripple and the proposal of a three-step procedure to tackle the design of the balancing feedback. The findings are supported by simulations and experimental results.**

***Index Terms*—Modeling, modular multilevel converters, nonlinear systems, perturbation methods.**

I. Introduction

THE topology known as modular multilevel converter (MMC) has been introduced in the industry for medium voltage and high voltage applications. As one of its main advantages, the MMC allows an almost unrestricted number of series connected cells, which practically unlinks the rated voltage of the converter from the semiconductor devices' blocking voltage. On the downside, control is challenging and can usually be split in three parts: 1) ensuring that the voltages within each arm do not deviate too much from each other, 2) fulfilling the requirements of the load, and 3) taking care that each arm retains an equal share of the stored energy.

Manuscript received November 13, 2019; revised March 23, 2020 and May 18, 2020; accepted June 25, 2020. Date of publication July 9, 2020; date of current version September 22, 2020. This work was supported by the Deutsche Forschungsgemeinschaft, DFG, under Grant GE 2502/5-1. Recommended for publication by Associate Editor M. Saeedifard. *(Corresponding author: Albrecht Gensior.)*

The authors are with the Professur Leistungselektronik, Elektrotechnisches Institut, Technische Universität Dresden, 01069 Dresden, Germany (e-mail: albrecht.gensior@tu-dresden.de; hendrik.fehr@mailbox.tu-dresden.de).

Color versions of one or more of the figures in this article are available online at https://ieeexplore.ieee.org.

Digital Object Identifier 10.1109/TPEL.2020.3008317

The first task is usually solved by a modulation algorithm or insertion index calculation that receives as reference the voltage to be realized across all cells of an arm, e.g., [1]–[9]. Depending on the direction of the current and possibly other information the cells to be inserted, bypassed, or modulated are selected. Depending on the algorithm used, the solution of the first task may solve the third task implicitly when the voltage errors generated by the modulation algorithm introduce a desired damping [10]–[14]. However, it slightly impairs the second task [15] and its balancing performance depends on operating conditions [16]. Using the measured capacitor voltages avoids this problem by minimizing the modulation voltage error but requires an explicit balancing controller [10], [11]. This is considered here. Applications can be found in loads sensitive to modulation voltage errors or to deviations of the desired load current waveform such that they benefit from a high modulation accuracy and a dedicated closed-loop current control. In any case, the cells of one arm can be modeled by one equivalent cell in the context of the remaining one or two tasks. While the first task can be solved somehow independently from the others, the second and optionally third task are usually treated together. However, a trajectory tracking control for all system variables is difficult because the system proves to be underactuated. This means there remains an internal dynamics of at least order two, which has been pointed out in [17] for instance. As a direct approach to deal with this problem, the methods developed in [18] and [19] predict the internal dynamics in order to find suitable reference trajectories. Although yielding good results, this option often appears too elaborate for the practical needs.

Fortunately, for many practical applications the energies are not required to follow specific trajectories as it is the case for the load currents for instance. Instead, it is sufficient to ensure that their averages reach their setpoints within a few periods of the base frequency. According to the overwhelming majority of references, the state-of-the-art solution for this problem employs dedicated frequency components in the circulating current and common-mode voltage. In an averaged sense and in conjunction with the ac voltage, dc voltage, or the output current, each component generates an additional power affecting a different energy. The roles of these components need to be identified for each relevant operating condition, which is usually done by analytic evaluation of the power introduced in the equivalent cells. This scheme has been applied successfully for different applications and operating regimes. In [20], drive applications

have been considered. In case of grid applications, this concept has been extended in [21] and [22] to consider also a negative sequence in the grid voltages. Optionally, balancing can be obtained in conjunction with a third-harmonic injection of the common-mode voltage as in [23]. In [24] the approach has been applied even in case of a nonconstant dc voltage. Generalizations that aim to include other converters are proposed in [25] and [26].

Although this approach is widely accepted, there are several drawbacks or open issues associated with it.

1) Its main drawback is that it does not provide a dynamic model for the average of the energies that is derived from the model equations of the electrical circuit. As a consequence, it is neither possible to choose an error dynamics for the balancing process nor to identify disturbances that may be compensated for in the controller design. As an exception, the authors in [22] state a model for the average quantities, but without a mathematical justification.
2) Furthermore, the approach assumes constancy of the components used for balancing which obviously contradicts the use of a balancing controller. Thus, although a certain decoupling can be observed for constant coefficients, this cannot be fulfilled during the balancing phase. This leads to undesired couplings that interfere with the balancing. As a recourse for this problem, the balancing speed must be limited. However, studies are missing that assess the extent of this limitation to explore the range of useful application. As an exception, see [27].
3) Usually, the discussion is limited to a particular application except for the approach in [25] which, however, suffers from the first two points. Thus, there is no general framework available that provides the versatility to tackle different applications with the same model.

Although dynamic phasor models as in [28]–[30] or models derived using harmonic state space approach as in [31]–[33] are capable to describe the behavior of the averaged voltages and do not assume constancy of the components, they increase the order of the system. Thus, they are better suited to model the closed loop when a balancing controller already exists rather than facilitating balancing control design.

Summing up, the modeling part required for a systematic model-based controller design for the energy balancing task has not been covered sufficiently yet.

The present article contributes to close this gap by presenting a modeling framework which employs singular perturbation methods in order to separate between the fast and the slow behavior of the system variables. In a first step, a rather standard method is used which leads to a current-fed model. In a second step and as one of the main contributions of the article, a lemma of singular perturbation theory for quasi-periodic systems from [34] is applied which is rather unknown in power electronics. The result is a mathematically backed model which lends itself to balancing control design, as it solely describes the average of the energies and allows to obtain a controller by specifying the error dynamics for the balancing task. As a side-effect, it allows to justify the findings of [20]–[22] in terms of the roles the spectral components of the currents play for balancing as well as the results from [35]–[40] discussing the impact of the components that do not influence the balancing but the voltage ripple. Beyond that, the approach opens up the way for other applications and operating regimes.

As a further contribution, a workflow for designing and implementing a controller is proposed that allows to stabilize the average of the energies with a prescribed error dynamics. Although the concept is very versatile, for the purpose of illustration and to relate the findings to the literature, it is applied to a standard application which leads to a well-known control approach. The same framework is then used to identify and avoid a singularity in this solution in a way which cannot be found in the literature so far. In order to explore its range of application, the impact of the mutual interactions are evaluated via simulation and measurements, revealing a tradeoff between model accuracy and balancing speed, that is inherent to any similar balancing scheme.

The article is organized as follows. The following Section II recalls a lemma of singular perturbation theory in a rather general form. It is applied to the MMC model in Section III in order to derive a dynamic model for the averaged quantities. Together with the description of the stationary operating regimes in Section IV, this enables the design of a controller in Section V. Since it is necessary to translate the controller from one modeling context to another, this is discussed in Section VI. Section VII is devoted to support the findings by simulation and experimental results. Finally, Section VIII concludes the article. The appendix briefly discusses a modeling step that enables to neglect the dynamics of the currents by making use of another method of singular perturbation theory.

II. Recall of a Singular Perturbation Method for Quasi-Periodic Systems

Since the article will exploit a lemma for quasi-periodic systems that can be found in, e.g., [34], it seems beneficial to recall this briefly. It considers systems of the form[1]

$$\dot{z} = \varepsilon f(t, z) + \varepsilon^2 g(t, z, \varepsilon) \tag{1}$$

fulfilling the following conditions:

1) The functions in the vector f are periodic in t with the period T. The average of f is

$$f^0(z) = \int_0^T f(t, z)\mathrm{d}t \tag{2}$$

where z is kept constant.
2) Functions f, g, and $\partial f/\partial z$ are continuous and bounded by a constant M independent of ε.
3) Function g is Lipschitz-continuous in z.

In this case the solution of

$$\dot{\bar{z}} = \varepsilon f^0(\bar{z}) \tag{3}$$

approximates the solution of (1) for identical initial conditions.

Another reference is [41] covering the case $g = 0$ only.

[1]Dot-notation $\dot{z}$ indicates the time derivative $\frac{\mathrm{d}}{\mathrm{d}t}z$

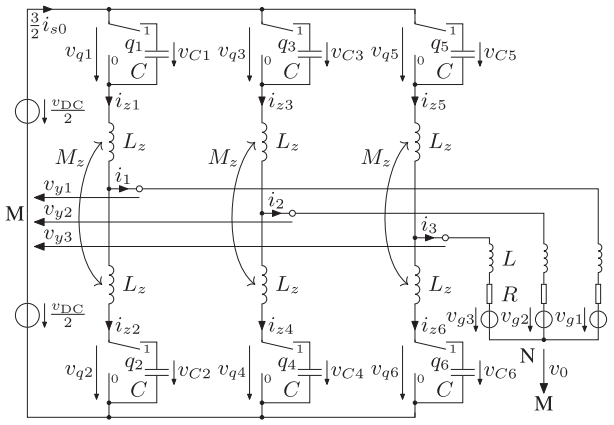

Fig. 1. Continuous model of an MMC with equivalent cells and inductive load with e.m.f. and isolated star point.

III. Modeling of an MMC

A. Circuit Model and Preliminary Steps

In order to ease the derivation of the model, the variables are considered as averaged quantities over the switching period. This is common practice and, in particular, causes the switching functions of the cells to cover the interval [0, 1]. Furthermore, the series connection of n cells per arm is replaced by an equivalent cell [42]–[44].[2] With these simplifications in mind, consider the MMC in Fig. 1. The modeling of the converter and the load can be done separately. Using the arm energy definition [27], [47]

$$e_{zk} = \frac{1}{2}Cv_{Ck}^2 + \frac{1}{2}(L_z + M_z)i_{zk}^2 - \frac{1}{4}M_z i_p^2$$
$$p = \left\lceil \frac{k}{2} \right\rceil, k = 1, \ldots, 6 \tag{4}$$

and the transformations and definitions in Table I, the model of the transformed MMC energies in stationary coordinates reads[3]

$$\frac{\mathrm{d}}{\mathrm{d}t}e_{s0} = v_{\mathrm{DC}}i_{s0} - \mathrm{Re}\big(\underline{i}\,\underline{v}_y^*\big) \tag{5a}$$
$$\frac{\mathrm{d}}{\mathrm{d}t}e_{d0} = -2v_{y0}i_{s0} - \mathrm{Re}\big(\underline{i}_s^*\underline{v}_{y\Delta}\big) \tag{5b}$$
$$\frac{\mathrm{d}}{\mathrm{d}t}\underline{e}_s = v_{\mathrm{DC}}\underline{i}_s - \underline{v}_y^*\underline{i}^* - 2\underline{i}\,v_{y0} \tag{5c}$$
$$\frac{\mathrm{d}}{\mathrm{d}t}\underline{e}_d = v_{\mathrm{DC}}\underline{i} - \underline{i}_s^*\underline{v}_{y\Delta}^* - 2\underline{i}_s v_{y0} - 2i_{s0}\underline{v}_{y\Delta} \tag{5d}$$

with

$$\underline{v}_{y\Delta} = \underline{v}_y - M_z\frac{\mathrm{d}}{\mathrm{d}t}\underline{i}. \tag{6}$$

The dynamics of the MMC currents reads

$$(L_z + M_z)\frac{\mathrm{d}}{\mathrm{d}t}i_{s0} = v_{x0} \tag{7a}$$
$$(L_z + M_z)\frac{\mathrm{d}}{\mathrm{d}t}\underline{i}_s = \underline{v}_x. \tag{7b}$$

Subsystem (5a) is a power balance between the stored energy e_{s0} and the dc side and ac side. The other subsystems describe the energy distribution among the arms. Details on the modeling can be found in [27] and [47]. Inclusion of the arm inductor in the energy definition (4) leads to a cascaded structure of the model, since the driving voltages v_{x0} and $\underline{v}_x$ of the currents do not appear in the energy system (5) [18].

TABLE I
Definitions and Transformations of Arm Energies, Currents and Voltages for the Circuit in Fig. 1

definition	description
$\boldsymbol{e}_z^+ = (e_{z1}, e_{z3}, e_{z5})^{\mathrm{T}}$	positive dc terminal arm energies
$\boldsymbol{e}_z^- = (e_{z2}, e_{z4}, e_{z6})^{\mathrm{T}}$	negative dc terminal arm energies
$\boldsymbol{g}_0 = \frac{1}{3}(1,1,1)$	zero sequence component
$\underline{\boldsymbol{g}}_{\alpha\beta} = \frac{2}{3}\left(1, \mathrm{e}^{\mathrm{j}\frac{2\pi}{3}}, \mathrm{e}^{-\mathrm{j}\frac{2\pi}{3}}\right)$	3ph axes in complex $\alpha\beta$ notation
$e_{s0} = 2\boldsymbol{g}_0(\boldsymbol{e}_z^+ + \boldsymbol{e}_z^-)$	stored energy (scaled)
$e_{d0} = 2\boldsymbol{g}_0(\boldsymbol{e}_z^+ - \boldsymbol{e}_z^-)$	vertical difference (scaled)
$\underline{e}_s = 2\underline{\boldsymbol{g}}_{\alpha\beta}(\boldsymbol{e}_z^+ + \boldsymbol{e}_z^-)$	complex energy sum
$\underline{e}_d = 2\underline{\boldsymbol{g}}_{\alpha\beta}(\boldsymbol{e}_z^+ - \boldsymbol{e}_z^-)$	complex energy difference
$\boldsymbol{i}_z^+ = (i_{z1}, i_{z3}, i_{z5})^{\mathrm{T}}$	positive dc terminal arm currents
$\boldsymbol{i}_z^- = (i_{z2}, i_{z4}, i_{z6})^{\mathrm{T}}$	negative dc terminal arm currents
$i_{s0} = \boldsymbol{g}_0(\boldsymbol{i}_z^+ + \boldsymbol{i}_z^-)$	(scaled) dc current
$\underline{i}_s = \underline{\boldsymbol{g}}_{\alpha\beta}(\boldsymbol{i}_z^+ + \boldsymbol{i}_z^-)$	complex circulating current
$\underline{i} = \underline{\boldsymbol{g}}_{\alpha\beta}(\boldsymbol{i}_z^+ - \boldsymbol{i}_z^-)$	complex output current
$\boldsymbol{v}_y = (v_{y1}, v_{y2}, v_{y3})^{\mathrm{T}}$	output voltages referred to M
$\boldsymbol{v}_q^+ = (v_{q1}, v_{q3}, v_{q5})^{\mathrm{T}}$	upper arm injected voltages
$\boldsymbol{v}_q^- = (v_{q2}, v_{q4}, v_{q6})^{\mathrm{T}}$	lower arm injected voltages
$\underline{v}_y = \underline{\boldsymbol{g}}_{\alpha\beta}\boldsymbol{v}_y$	complex output voltage
$v_{y0} = \boldsymbol{g}_0\boldsymbol{v}_y$	common-mode voltage referred to M
$v_{x0} = v_{\mathrm{DC}} - \boldsymbol{g}_0(\boldsymbol{v}_q^+ + \boldsymbol{v}_q^-)$	dc current driving voltage
$\underline{v}_x = -\underline{\boldsymbol{g}}_{\alpha\beta}(\boldsymbol{v}_q^+ + \boldsymbol{v}_q^-)$	circulating current driving voltage
$\boldsymbol{v}_g = (v_{g1}, v_{g2}, v_{g3})^{\mathrm{T}}$	load voltages
$\underline{v}_g = \underline{\boldsymbol{g}}_{\alpha\beta}\boldsymbol{v}_g$	complex load voltage
$v_{g0} = \boldsymbol{g}_0\boldsymbol{v}_g$	common-mode voltage of the load
$i_0 = \boldsymbol{g}_0(i_1, i_2, i_3)$	common-mode current of the load

For the model of the load one obtains

$$L\frac{\mathrm{d}}{\mathrm{d}t}\underline{i} = \underline{v}_y - R\underline{i} - \underline{v}_g \tag{8a}$$
$$v_0 = v_{y0} - v_{g0} \tag{8b}$$
$$i_0 = 0 \tag{8c}$$

in the transformed variables from Table I.

For modeling purposes, the modulation algorithm is assumed to ideally inject the arm voltage v_{qk} implying a modulation that takes the available voltage into account, e.g., [48]. However, a voltage error can easily be included in the model to cover other control approaches.

The model used here differs from other models, e.g., [10], [28]–[30], in terms of using the energies rather than the capacitor voltages as coordinates. However, it also differs from energy models in most other references, [22], [49], [50] for instance, by incorporating the energy stored in the inductors as can be seen from (4). Although the quantitative impact is low, it leads to a more compact model and avoids the neglect of terms related to the energy exchange with the inductors. In [49] and [50] for instance, these terms have been neglected by arguing that they are small.

Summing up, (5)–(7), and (8) describe the model of the MMC and its load, which is the point of departure for the subsequent modeling steps. Before continuing with these, it might be helpful to recall the difficulty of controlling MMCs by having a look at the quantities to be controlled and the inputs of the system:

[2]Details on the error introduced by this step can be found in [45] and [46] for instance.

[3]Note that for a complex variable $\underline{a}$, $\underline{a}^* = \mathrm{conj}(\underline{a})$.

Counting complex quantities as two, the model at this point consists of equations in six arm energies, two load currents, two circulating currents, the dc-current, and six voltages corresponding to the duty-cycles for the equivalent cells serving as inputs. The requirements of the load fix the trajectory of the complex load current $\underline{i}$ whose closed-loop control consumes the input $\underline{v}_y$. The energy e_{s0} is controlled via the dc-current which in turn is controlled by v_{x0}. Either $\underline{e}_s$ or $\underline{e}_d$ can be controlled by the circulating current $\underline{i}_s$ via $\underline{v}_x$. Finally, the common-mode voltage v_{y0} can be used to control e_{d0}. Thus, two real-valued energies are left uncontrolled. In other words, dedicating the load current control solely to the application, generally requires an explicit balancing scheme.

This motivates to develop another model not suffering from being underactuated which proceeds in Section III-C. Before doing so, a rather standard method of singular perturbations theory is used to replace the currents by their quasi-stationary counterparts.

B. Dealing With the Dynamics of the Currents

At least from a heuristic point of view it is common practice to neglect the dynamics of the fast subsystem when discussing the dynamics of the slow subsystem if such a splitting seems appropriate at all. For MMCs, this means disregarding the dynamics of the currents when dealing with the dynamics of the energies. This leads to the simplified model

$$\tfrac{\mathrm{d}}{\mathrm{d}t}e_{s0} = v_{\mathrm{DC}}i_{s0} - \mathrm{Re}\big(\underline{i}\,\underline{v}_y^*\big) \tag{9a}$$

$$\tfrac{\mathrm{d}}{\mathrm{d}t}e_{d0} = -2v_{y0}i_{s0} - \mathrm{Re}\big(\underline{i}_s^*\underline{v}_y\big) \tag{9b}$$

$$\tfrac{\mathrm{d}}{\mathrm{d}t}\underline{e}_s = v_{\mathrm{DC}}\underline{i}_s - \underline{v}_y^*\underline{i}^* - 2\underline{i}\,v_{y0} \tag{9c}$$

$$\tfrac{\mathrm{d}}{\mathrm{d}t}\underline{e}_d = v_{\mathrm{DC}}\underline{i} - \underline{i}_s^*\underline{v}_y^* - 2\underline{i}_s v_{y0} - 2i_{s0}\underline{v}_y. \tag{9d}$$

This procedure can be justified by applying a rather standard method of singular perturbation theory as shown in the Appendix.

However, although reduced by the dynamics of the currents, the system is still underactuated. Furthermore, there do not exist meaningful nontrivial stationary operating points in the sense that all derivatives on the left-hand side of (9) vanish. Although this can be avoided in an elegant way by choosing dedicated reference frames for each energy, it may lead to restrictions regarding the operation because this allows only for one frequency component in each energy. This can be seen in [50], for instance, where $\underline{i}_s$ allows only for a single harmonic of minus twice the base frequency and $v_{y0} = 0$. In order to avoid such limitations, the present article rather focuses on stationary operating regimes where the solutions of (9) are periodical in time, possibly containing more than one frequency component. The modeling step proceeding next will help to identify such regimes and provide a model that does not suffer from being underactuated. Therefore, (9) serves as starting point.

C. Averaged Model

In a usual application of an MMC, the trajectories of the quantities on the right-hand side of (9) can be described by the Fourier series

$$\underline{v}_y = \underline{V}_y^{[1]}\mathrm{e}^{\mathrm{j}\omega t} + \underline{V}_y^{[-1]}\mathrm{e}^{-\mathrm{j}\omega t} \tag{10a}$$

$$\underline{i} = \underline{I}^{[1]}\mathrm{e}^{\mathrm{j}\omega t} + \underline{I}^{[-1]}\mathrm{e}^{-\mathrm{j}\omega t} \tag{10b}$$

$$v_{y0} = V_{y0}^{[0]} + \sum_{k\in\mathbb{Z}\setminus\{0\}} \underline{V}_{y0}^{[k]}\mathrm{e}^{\mathrm{j}k\omega t} \tag{10c}$$

$$v_{\mathrm{DC}} = V_{\mathrm{DC}}^{[0]} \tag{10d}$$

$$i_{s0} = I_{s0}^{[0]} + \sum_{k\in\mathbb{Z}\setminus\{0\}} \underline{I}_{s0}^{[k]}\mathrm{e}^{\mathrm{j}k\omega t} \tag{10e}$$

$$\underline{i}_s = \sum_{k\in\mathbb{Z}} \underline{I}_s^{[k]}\mathrm{e}^{\mathrm{j}k\omega t} \tag{10f}$$

with $\omega = \mathrm{const}$. The assumption of constancy of the angular frequency is justified here since the focus lies on a grid-connected system. Some of the coefficients in (10) have already been omitted because in the present context they are negligible in practice. Since the remaining coefficients are complex, they inherently contain the information about the phase alignment. However, for the load positive and negative sequences for voltages and currents are still possible. Since v_{y0} and i_{s0} are real quantities, $\underline{V}_{y0}^{[-k]} = \underline{V}_{y0}^{[k]\,*}$ and $\underline{I}_{s0}^{[-k]} = \underline{I}_{s0}^{[k]\,*}$ hold for $k = 1, 2, \ldots, \infty$. This representation is beneficial for the calculations below.

In practice, the coefficients will change slowly in time which especially may be caused by a feedback, which has yet to be determined. For the time being, it can be considered by a Taylor expansion $\underline{V}_y^{[1]}(t) = \underline{V}_{y,(0)}^{[1]} + \underline{V}_{y,(1)}^{[1]}t + \ldots$ with $\underline{V}_{y,(0)}^{[1]}, \underline{V}_{y,(1)}^{[1]}, \ldots = \mathrm{const}$ in the case of $\underline{V}_y^{[1]}$ and similarly for the other coefficients.

Inserting the assumptions (10) on the right-hand side of (9) and changing the time as $\tau = \omega t$ brings (9) in the form (1). The perturbation parameter is $\varepsilon = \omega^{-1}$. Considering the time dependence of the coefficients, it turns out that $\underline{V}_{y,(0)}^{[1]}$ and its counterparts appear in f, and $\underline{V}_{y,(i)}^{[1]}$, $i = 1, 2, \ldots$ and the corresponding coefficients of the other quantities appear in g. If one assumes constant coefficients in (10) which is equivalent to terminating the Taylor series after the zeroth element, g vanishes. This case is also covered by [41]. Thus, it turns out that the series used for the coefficients enables to consider that they depend on time which brings the system in the form (1) with $g \neq 0$ such that the theorem from [34] is applicable.

Following the results from [34] (see Section II), an approximation can be obtained by averaging f over $\tau \in [0, 2\pi]$. This eliminates all terms with arguments depending on τ. In the original time t, this yields the simplified model[4]

$$\tfrac{\mathrm{d}}{\mathrm{d}t}\bar{e}_{s0} = V_{\mathrm{DC}}^{[0]}I_{s0}^{[0]} - \mathrm{Re}\Big(\underline{I}^{[1]}\underline{V}_y^{[1]\,*} + \underline{I}^{[-1]}\underline{V}_y^{[-1]\,*}\Big) \tag{11a}$$

$$\begin{aligned}\tfrac{\mathrm{d}}{\mathrm{d}t}\bar{e}_{d0} = &-2I_{s0}^{[0]}V_{y0}^{[0]} - \sum_{k\in\mathbb{Z}\setminus\{0\}} 2\underline{I}_{s0}^{[k]}\underline{V}_{y0}^{[-k]} \\ &- \mathrm{Re}\Big(\underline{V}_y^{[1]}\underline{I}_s^{[1]\,*} + \underline{V}_y^{[-1]\,*}\underline{I}_s^{[-1]}\Big)\end{aligned} \tag{11b}$$

[4]Consider that for two complex variables $\underline{a}, \underline{b}$ it holds $\underline{a}\underline{b}^* + \underline{a}^*\underline{b} = 2\mathrm{Re}(\underline{a}\underline{b}^*)$.

$$\frac{\mathrm{d}}{\mathrm{d}t}\underline{\bar{e}}_s = V_{\mathrm{DC}}^{[0]}\,\underline{I}_s^{[0]} - \underline{V}_y^{[-1]^*}\underline{I}^{[1]^*} - 2\underline{I}^{[1]}\,\underline{V}_{y0}^{[-1]} - \underline{V}_y^{[1]^*}\underline{I}^{[-1]^*} - 2\underline{I}^{[-1]}\,\underline{V}_{y0}^{[1]} \tag{11c}$$

$$\frac{\mathrm{d}}{\mathrm{d}t}\underline{\bar{e}}_d = -\underline{V}_y^{[-1]^*}\underline{I}_s^{[1]^*} - \underline{V}_y^{[1]^*}\underline{I}_s^{[-1]^*} - 2\sum_{k\in\mathbb{Z}}\underline{V}_{y0}^{[-k]}\underline{I}_s^{[k]} - 2\underline{V}_y^{[-1]}\underline{I}_{s0}^{[1]} - 2\underline{V}_y^{[1]}\underline{I}_{s0}^{[-1]}. \tag{11d}$$

Note that the same model is obtained no matter whether the coefficients are constant ($g = 0$) or slowly changing (g nonzero). This is why the case with time-dependent coefficients is covered as well. Thus, in order to ease the notation, the coefficients have been named as in (10) when they are considered to be constant. However, keep in mind that the disregard of g by the theorem leads to a modeling error. Thus, the obtained model is an approximation that is valid only to a limited extend. In Section VII-B, experiments will be performed in order to explore the limits of validity of the model.

Besides the fact that [28]–[30] use voltages instead of energies as state variables, the model (11) is linked to the dynamic phasor models in a way that it only describes the component with index zero, i.e., the dc part. The same applies to the models in [31]–[33] which use a similar concept known as harmonic state space modeling. Although these models are well suited to describe the behavior of the system when a controller already exists, it is difficult to use them for control design because they artificially increase the order of the resulting model and create the problem of obtaining these states from the six energies of the MMC. In contrast, the purpose of the present model is to facilitate the control design.

D. Properties of the Model (11)

In contrast to the original model (9), describing the instantaneous behavior of the system, the model (11) describes the behavior of the system in an averaged sense. As a consequence, it exhibits fundamentally different properties at least in the following two points.

First off, it has meaningful stationary operating points which can be identified by setting the left-hand side to zero, similar to the models in [28] for a different converter. Such stationary operating points of (11) correspond to stationary operating regimes of (9). This is discussed in more detail in Section IV.

Second, depending on the application and control engineering considerations, some of the coefficients in (10) will be *parameters* while others will be *system variables*.[5] Since there may appear products of system variables on the right-hand side of (11), in general, the system is nonlinear. Thus, it evades from checking the controllability as it can be done for linear systems. Fortunately, the property of differential flatness extends the concept of controllability to nonlinear systems. A system is differentially flat, if all system variables can be parameterized by trajectories of a so-called flat output [51]. Interestingly, the energies do not appear on the right-hand side of (11). Furthermore, in any case they will be part of the set of system variables which means that $y = (\bar{e}_{s0}, \bar{e}_{d0}, \underline{\bar{e}}_s, \underline{\bar{e}}_d)$ will be the only reasonable candidate for a flat output. Proving for flatness reduces then to solving for the remaining system variables. Since different coefficients of the same variable in the reduced model (9) can be assigned the role of system variables, in practice, one will extend the system by algebraic constraints. These equations become part of the model and ensure that a unique solution can still be found. This process is part of the control design which is discussed in Section V.

[5]Modeling quantities that are fixed by external requirements or by assumptions will be called parameters in this text. The remaining quantities are system variables.

IV. Stationary Regimes of the Reduced Model

A. General Idea

Assuming a stationary regime of the load, given by (10a) and (10b), stationary operating regimes of the reduced model (9) can be found by setting the left-hand side of (11) to zero. Since this possibly does not fix all coefficients in the series expansions (10c)–(10f) yet, further requirements can be incorporated as demonstrated by an example below. Depending on these choices, one obtains different possible regimes which can be expressed by sums of complex exponentials

$$e_{s0} = E_{s0}^{[0]} + \underbrace{\sum_{k\in\mathbb{N}} \mathrm{Re}\left(\underline{E}_{s0}^{[k]}\mathrm{e}^{\mathrm{j}k\omega t}\right)}_{e_{s0,\mathrm{AC}}} \tag{12a}$$

$$e_{d0} = E_{d0}^{[0]} + \underbrace{\sum_{k\in\mathbb{N}} \mathrm{Re}\left(\underline{E}_{d0}^{[k]}\mathrm{e}^{\mathrm{j}k\omega t}\right)}_{e_{d0,\mathrm{AC}}} \tag{12b}$$

$$\underline{e}_s = \underline{E}_s^{[0]} + \underbrace{\sum_{k\in\mathbb{Z}\setminus\{0\}} \underline{E}_s^{[k]}\mathrm{e}^{\mathrm{j}k\omega t}}_{\underline{e}_{s,\mathrm{AC}}} \tag{12c}$$

$$\underline{e}_d = \underline{E}_d^{[0]} + \underbrace{\sum_{k\in\mathbb{Z}\setminus\{0\}} \underline{E}_d^{[k]}\mathrm{e}^{\mathrm{j}k\omega t}}_{\underline{e}_{d,\mathrm{AC}}}. \tag{12d}$$

The dc offset $E_{s0}^{[0]}$ in the stored energy e_{s0} determines the average cell capacitor voltage and needs to be higher than $2Cv_{\mathrm{DC}}^2$, i.e., the value required to block the dc voltage with just one arm, in order to provide enough room for the ac components of the cell voltages. The dc offsets in the other energies, i.e., $E_{d0}^{[0]}$, $\underline{E}_s^{[0]}$, and $\underline{E}_d^{[0]}$, are zero in a balanced regime. The coefficients with $k \neq 0$ of the stationary regime (12) represent the ac components of the energies.

B. Example

A popular operating regime for symmetrical grid conditions is characterized by a constant dc voltage, a constant dc current, an optional *triplen harmonic injection* of the common-mode voltage, and either zero circulating current or using a second harmonic instead, which boils down to the coefficients

$$\underline{I}^{[-1]} = 0 \tag{13a}$$

$$\underline{V}_y^{[-1]} = 0 \tag{13b}$$

TABLE II
CONSTANTS OF THE EXAMPLE STATIONARY OPERATING REGIME CORRESPONDING TO (13a), (13b), (13e)–(13g). THE SHADED PART IN $\underline{E}_s^{[-2]}$ VANISHES BY CHOOSING (13c) WITH $A = 1$

$E_{s0}^{[0]}$	$> 2Cv_{\mathrm{DC}}^2$
$\mathrm{j}\omega\underline{E}_{d0}^{[3]}$	$-\frac{4}{3}I_{s0}^{[0]}\underline{V}_{y0}^{[3]} - \frac{1}{3}\underline{V}_y^{[1]}\underline{I}_s^{[-2]*}$
$\mathrm{j}\omega\underline{E}_s^{[-2]}$	$\frac{1}{2}\underline{V}_y^{[1]*}\underline{I}^{[1]*} - \frac{1}{2}\underline{V}_{\mathrm{DC}}^{[0]}\underline{I}_s^{[-2]} + \underline{I}^{[1]}\underline{V}_{y0}^{[3]*}$
$\mathrm{j}\omega\underline{E}_s^{[4]}$	$-\frac{1}{2}\underline{I}^{[1]}\underline{V}_{y0}^{[3]}$
$\mathrm{j}\omega\underline{E}_d^{[-5]}$	$\frac{2}{5}\underline{I}_s^{[-2]}\underline{V}_{y0}^{[3]*}$
$\mathrm{j}\omega\underline{E}_d^{[1]}$	$V_{\mathrm{DC}}^{[0]}\underline{I}^{[1]} - 2I_{s0}^{[0]}\underline{V}_y^{[1]} - \underline{I}_s^{[-2]*}\underline{V}_y^{[1]*} - 2\underline{I}_s^{[-2]}\underline{V}_{y0}^{[3]}$
all other	0

TABLE III
PARAMETERS OF THE MMC FOR THE EXPERIMENTS

	symbol	value
number of cells per arm	n	6
cell capacitance	nC	375 µF
arm inductor	L_z	1.2 mH
mutual inductance	M_z	0.94 mH
rated arm current peak	$\hat{I}$	25 A
nominal dc-voltage	$V_{\mathrm{DC,r}}$	650 V
controller sampling rate and PWM frequency		4.884 kHz
measurement to PWM update delay		102.4 µs
average power device switching frequency [53]	f_{avg}	857 Hz

$$\underline{I}_s^{[k]} = \begin{cases} \frac{A}{V_{\mathrm{DC}}^{[0]}}\underline{I}^{[1]*}\underline{V}_y^{[1]*} & k = -2 \\ 0 & \text{otherwise} \end{cases} \tag{13c}$$

$$\underline{V}_{y0}^{[k]} = \begin{cases} -\frac{1}{12}|\underline{V}_y^{[1]}|\mathrm{e}^{\mathrm{j}k\arg\underline{V}_y^{[1]}} & k = -3, 3 \\ 0 & \text{otherwise} \end{cases} \tag{13d}$$

$$V_{\mathrm{DC}}^{[0]} > |\underline{v}_y|\sqrt{3} \tag{13e}$$

$$I_{s0}^{[0]} = \frac{1}{V_{\mathrm{DC}}^{[0]}}\mathrm{Re}\left(\underline{V}_y^{[1]}\underline{I}^{[1]*}\right) \tag{13f}$$

$$I_{s0}^{[k]} = 0, \quad k \geq 1. \tag{13g}$$

The variable $A \in \{0, 1\}$ in (13c) acts as a switch to optionally compensate the second power term on the right hand side of (9c) which reduces the cell capacitor voltage ripple amplitude, as in [35]–[40], [52].

The conditions (13) constitute a stationary solution of the averaged system (11), because they render to zero its right-hand side. The energy variables of the nonaveraged system (9) assume the shape of (12) in which the constants $\underline{E}_{d0}^{[3]}$, $\underline{E}_s^{[-2]}$, $\underline{E}_s^{[4]}$, $\underline{E}_d^{[-5]}$, and $\underline{E}_d^{[1]}$ appear as given in Table II.

Representative waveforms of the regime (13) are given in Fig. 2 for both values of A using the parameter set given in Table III characterizing the test bench used for the experiments. The dc voltage $V_{\mathrm{DC}}^{[0]}$, output current $\underline{I}^{[1]}$, and output voltage $\underline{V}_y^{[1]}$ are the same for both cases and given in Table IV. Note that the generation of the plots does not require a simulation (i.e., a numerical solution of differential equations) because the solutions

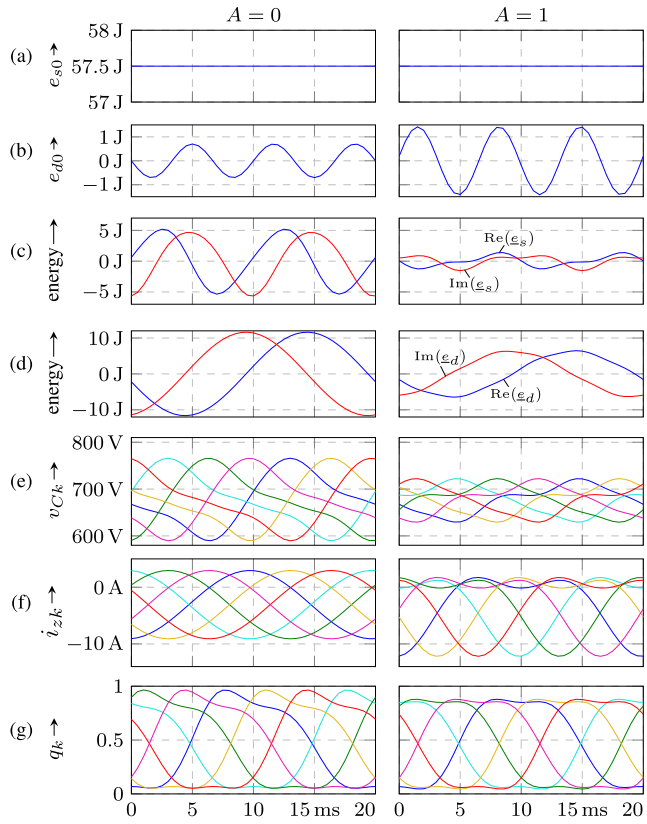

Fig. 2. Example regime (13) for $A = 0$ (left) and $A = 1$ (right): (a) Stored energy e_{s0}, (b) vertical difference e_{d0}, (c) complex sum $\underline{e}_s$, (d) complex difference $\underline{e}_d$, (e) equivalent cell voltages v_{Ck}, (f) arm currents i_{zk}, (g) duty-cycles q_k, $k = 1, \ldots, 6$. The MMC parameters are given in Table III and $V_{\mathrm{DC}}^{[0]}$, $\underline{I}^{[1]}$, $\underline{V}_y^{[1]}$, and ω can be found in Table IV.

TABLE IV
PARAMETERS USED IN THE CALCULATIONS, SIMULATIONS, AND MEASUREMENTS

variable	symbol	value	Figs.
output voltage	$\underline{V}_y^{[1]}$	323 V	2, 9–12
dc voltage	$V_{\mathrm{DC}}^{[0]}$	630 V	—"—
		645 V	13
output current	$\underline{I}^{[1]}$	$(-12 - \mathrm{j}1.1)$ A	2, 9–12
stored energy reference	$\bar{e}_{s0,\mathrm{ref}}$	81.28 J	9–12
		55 J	13
angular frequency	ω	$2\pi 50$ Hz	2, 9–13
e_{s0}-control gain	$l_{s0}/V_{\mathrm{DC}}^{[0]}$	$1.5\,\mathrm{V}^{-1}\,\mathrm{s}^{-1}$	9–13
e_{s0}-control integral gain	$l_{s0,I}/V_{\mathrm{DC}}^{[0]}$	$323\,\mathrm{V}^{-1}\,\mathrm{s}^{-2}$	9–13
gain setting Case A	l_{d0}, l_s, l_d	$50\,\mathrm{s}^{-1}$	9–12
gain setting Case B	—"—	$122\,\mathrm{s}^{-1}$	11–13
gain setting Case C	—"—	$400\,\mathrm{s}^{-1}$	11, 12

can be calculated directly from (12) with the coefficients from Table II and the use of the inverse of the transforms given in Table I to obtain the quantities in natural coordinates.

The regime is similar to the *hf-mode* in [20] except for the complex notation. The coefficients $\underline{V}_{y0}^{[\pm 3]}$ in Table II allow to emulate the *HB-B approach* in [22] by disabling the third-harmonic common-mode voltage via the setting $\underline{V}_{y0}^{[\pm 3]} = 0$.

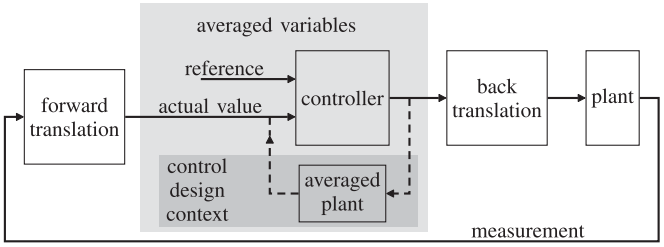

Fig. 3. Generic block diagram of a controller using averaged variables, indicated by the outer shaded region. The controller is designed using the dashed loop in the inner shaded region.

V. Control

A. General Idea

The shaded regions of the generic block diagram in Fig. 3 illustrate the simplifications that have been achieved by the previous modeling steps: The *averaged plant* represents the relevant behavior of the unshaded signal path through the real plant, allowing an efficient control design via the much simpler dashed loop. Obviously, a translation between the averaged and nonaveraged context is required, which is indicated by the blocks denoted *forward* and *back translation*, respectively.

The goal of the control design consists in designing a feedback law that stabilizes the trajectories of the averaged system (11) around their nominal ones $\bar{e}_{s0,\mathrm{ref}}$, $\bar{e}_{d0,\mathrm{ref}}$, $\underline{\bar{e}}_{s,\mathrm{ref}}$, and $\underline{\bar{e}}_{d,\mathrm{ref}}$. Usually these trajectories are constant which reduces the problem to the stabilization of a given stationary operating point; one of which has been discussed in Section IV-B. In general, the control design proceeds in the following steps.

1) Collection of System Variables: For an analysis of the model from a control engineering perspective it is necessary that each quantity in the model must be assigned the role of being either a parameter or a system variable. Those fixed by external requirements or by additional assumptions are parameters that can be collected in the set $\mathcal{P}$ and may have to be compensated for later. If not compensated, the parameter will act as a disturbance. The remaining quantities are denoted as system variables which can be collected in the set $\mathcal{V}$. Although they assume fixed values in a stationary regime, in the transient phase they may deviate from these values in order to accomplish the balancing task. Note that, due to the Fourier series, the cardinality of $\mathcal{V}$ might be infinite.

2) Control Input Assignment: The control of the six energies described by (11) requires six control variables that are collected in the tuple $u = (u_1, \ldots, u_6)$. The goal of this step is to assign the control inputs to the system variables in $\mathcal{V}$. Therefore, a mapping

$$v_i = g_i(u) \tag{14}$$

must be chosen, where $v_i \in \mathcal{V}$ and $g_i : \mathbb{R}^6 \to \mathbb{R}$. These equations become part of the model and the choice is valid, if it is possible to express all system variables in terms of the derivative of the output y, i.e., $\frac{\mathrm{d}}{\mathrm{d}t}y = (\frac{\mathrm{d}}{\mathrm{d}t}\bar{e}_{s0}, \frac{\mathrm{d}}{\mathrm{d}t}\bar{e}_{d0}, \frac{\mathrm{d}}{\mathrm{d}t}\underline{\bar{e}}_{s}, \frac{\mathrm{d}}{\mathrm{d}t}\underline{\bar{e}}_{d})$ which makes y a flat output of the system (11), (14). Thus, at least locally exist solutions of the form

$$u_k = h_k\left(\tfrac{\mathrm{d}}{\mathrm{d}t}\bar{e}_{s0}, \tfrac{\mathrm{d}}{\mathrm{d}t}\bar{e}_{d0}, \tfrac{\mathrm{d}}{\mathrm{d}t}\underline{\bar{e}}_{s}, \tfrac{\mathrm{d}}{\mathrm{d}t}\underline{\bar{e}}_{d}\right) \tag{15}$$

and one may proceed with the next step.

Note that in the simplest case, six system variables are picked out from the set $\mathcal{V}$ to define the components of the input u while the remaining variables from $\mathcal{V}$ are set to zero. Alternatively, additional requirements can be formulated at this stage that may lead to a more sophisticated choice of the functions g_i. As an example, it is possible to share the control effort among different system variables. In [26] this has been done in order to minimize the root mean square (rms) arm currents in a similar application.

Note further that if a function g_i is independent of u, this has essentially the same effect than assigning v_i the role of a parameter.

3) Error Dynamics Design: Finally, a desired dynamics for the errors $\bar{e}_{s0} - \bar{e}_{s0,\mathrm{ref}}$, $\bar{e}_{d0} - \bar{e}_{d0,\mathrm{ref}}$, $\underline{\bar{e}}_{s} - \underline{\bar{e}}_{s,\mathrm{ref}}$, and $\underline{\bar{e}}_{d} - \underline{\bar{e}}_{d,\mathrm{ref}}$ must be chosen. For instance, the dynamics

$$\tfrac{\mathrm{d}}{\mathrm{d}t}(\bar{e}_{s0} - \bar{e}_{s0,\mathrm{ref}}) = -l_{s0}(\bar{e}_{s0} - \bar{e}_{s0,\mathrm{ref}}) - l_{s0,I}\bar{e}_{s0,I} \tag{16a}$$

$$\tfrac{\mathrm{d}}{\mathrm{d}t}(\bar{e}_{d0} - \bar{e}_{d0,\mathrm{ref}}) = -l_{d0}(\bar{e}_{d0} - \bar{e}_{d0,\mathrm{ref}}) \tag{16b}$$

$$\tfrac{\mathrm{d}}{\mathrm{d}t}(\underline{\bar{e}}_{s} - \underline{\bar{e}}_{s,\mathrm{ref}}) = -l_{s}(\underline{\bar{e}}_{s} - \underline{\bar{e}}_{s,\mathrm{ref}}) \tag{16c}$$

$$\tfrac{\mathrm{d}}{\mathrm{d}t}(\underline{\bar{e}}_{d} - \underline{\bar{e}}_{d,\mathrm{ref}}) = -l_{d}(\underline{\bar{e}}_{d} - \underline{\bar{e}}_{d,\mathrm{ref}}) \tag{16d}$$

$$\tfrac{\mathrm{d}}{\mathrm{d}t}\bar{e}_{s0,I} = \bar{e}_{s0} - \bar{e}_{s0,\mathrm{ref}} \tag{16e}$$

with the controller parameters $l_{s0}, l_{s0,I}, l_{d0}, l_s, l_d$ enables an asymptotic decay of the energy errors. The integral gain $l_{s0,I}$ eliminates a remaining control error in the stored energy in case of model inaccuracies.

B. Example

For a better understanding, this is illustrated by an example:

1) Collection of System Variables: An operating regime is considered that complies with the regime introduced in Section IV-B.

In order to avoid any interference of the third-harmonic injection of the common-mode voltage and the optional second-harmonic injection of the circulating current with the controller design, $\underline{I}_s^{[\pm 3]} = 0$ and $\underline{V}_{y0}^{[2]} = 0$ rendering any contributions of these two quantities together with $\underline{V}_{y0}^{[\pm 3]}$ and $\underline{I}_s^{[-2]}$ irrelevant for the averaged behavior; see (11). Thus, the parameters and system variables are collected in the sets $\mathcal{P} = \{\underline{V}_y^{[1]}, \underline{V}_{y0}^{[2]}, \underline{V}_{y0}^{[\pm 3]}, \underline{I}^{[1]}, \underline{V}_y^{[-1]}, \underline{I}_s^{[-2]}, \underline{I}_s^{[\pm 3]}, \underline{I}^{[-1]}, V_{\mathrm{DC}}^{[0]}\}$ and $\mathcal{V} = \{I_{s0}^{[0]}, \underline{I}_s^{[0]}, V_{y0}^{[0]}\} \bigcup \{\underline{I}_{s0}^{[k]}, \underline{I}_s^{[l]}, \underline{V}_{y0}^{[m]} | k \in \mathbb{Z} \setminus \{0\}, l \in \mathbb{Z} \setminus \{0, -2, \pm 3\}, m \in \mathbb{Z} \setminus \{0, 2, \pm 3\}\}$.

2) Control Input Assignment: Considering the assumptions from 1) in the model (11), one can see that there is only one term that is already fixed, namely, $\mathrm{Re}(\underline{I}^{[1]}\underline{V}_y^{[1]*})$ in (11a). Since on the right-hand side of (11a), only $I_{s0}^{[0]}$ belongs to the system variables, this one must be taken as a component of the input. However, there are five (real) quantities left and there are different options to choose the remaining components of the input u.

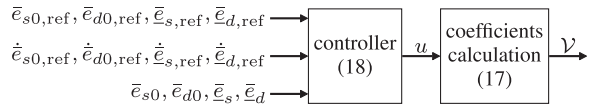

Fig. 4. Block diagram of the controller in terms of the averaged variables.

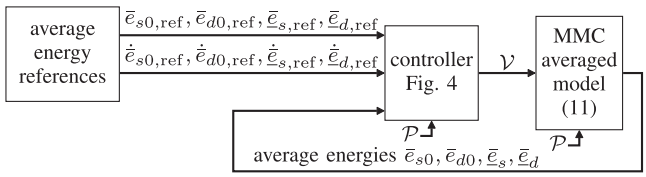

Fig. 5. Block diagram of the controller applied to the MMC averaged model (11).

A very popular choice for the mapping (14) is

$$I_{s0}^{[0]} = u_1 \tag{17a}$$

$$\underline{I}_{s}^{[1]} = u_2 \mathrm{e}^{\mathrm{j}\arg(\underline{V}_{y}^{[1]})} \tag{17b}$$

$$\underline{I}_{s}^{[0]} = u_3 + \mathrm{j}u_4 \tag{17c}$$

$$\underline{I}_{s}^{[-1]} = (u_5 + \mathrm{j}u_6)\mathrm{e}^{-\mathrm{j}\arg(\underline{V}_{y}^{[1]})} \tag{17d}$$

$$\underline{I}_{s}^{[k]} = 0, \quad k \in \mathbb{Z} \setminus \{-3, -2, -1, 0, 1, 3\} \tag{17e}$$

$$\underline{V}_{y0}^{[k]} = 0, \quad k \in \mathbb{Z} \setminus \{-3, 2, 3\} \tag{17f}$$

$$\underline{I}_{s0}^{[k]} = 0, \quad k \in \mathbb{Z} \setminus \{0\}, \tag{17g}$$

see [15] or Case A in [23]. [6]

3) Error Dynamics Design: The error dynamics (16) can be used to eliminate the derivatives of the energies in (15) leading to

$$u_1 = \tfrac{1}{V_{\mathrm{DC}}^{[0]}} \big(\tfrac{\mathrm{d}}{\mathrm{d}t} \bar{e}_{s0,\mathrm{ref}} - l_{s0}(\bar{e}_{s0} - \bar{e}_{s0,\mathrm{ref}}) - l_{s0,I}\bar{e}_{s0,I} + \mathrm{Re}\Big(\underline{I}^{[1]} \underline{V}_{y}^{[1]*} \Big) \big) \tag{18a}$$

$$u_2 = -\tfrac{1}{|\underline{V}_{y}^{[1]}|} \big(\tfrac{\mathrm{d}}{\mathrm{d}t} \bar{e}_{d0,\mathrm{ref}} - l_{d0}(\bar{e}_{d0} - \bar{e}_{d0,\mathrm{ref}}) \big) \tag{18b}$$

$$u_3 + \mathrm{j}u_4 = \tfrac{1}{V_{\mathrm{DC}}^{[0]}} \big(\tfrac{\mathrm{d}}{\mathrm{d}t} \underline{\bar{e}}_{s,\mathrm{ref}} - l_s(\underline{\bar{e}}_{s} - \underline{\bar{e}}_{s,\mathrm{ref}}) \big) \tag{18c}$$

$$u_5 + \mathrm{j}u_6 = -\tfrac{1}{|\underline{V}_{y}^{[1]}|} \big(\tfrac{\mathrm{d}}{\mathrm{d}t} \underline{\bar{e}}_{d,\mathrm{ref}}^{*} - l_d(\underline{\bar{e}}_{d}^{*} - \underline{\bar{e}}_{d,\mathrm{ref}}^{*}) \big) . \tag{18d}$$

As one can see, as long as $|\underline{V}_{y}^{[1]}| > 0$, the concept will work and, if desired, it is also possible to add integral parts as already suggested in (16a), (16e). A possibility to avoid this singularity is discussed later in Section VII-C. Besides the expected control of the stored energy by the dc current, the derived controller (18) implements the common horizontal and vertical energy balancing, e.g., [20], [22], [23]: Subsystem (18c) provides the horizontal balancing of the complex energy sum $\underline{e}_s$ via the dc component of the circulating current (17c). And, subsystems (18b) and (18d) provide the vertical balancing of the energy difference e_{d0} and $\underline{e}_d$ via the positive sequence (17b) and negative sequence (17d) circulating current, respectively.

The block diagram in Fig. 4 shows the resulting controller and the diagram in Fig. 5 depicts its application to the averaged system. The controller receives the average energy references, including, if desired, their derivatives, while its output u is inserted into the mapping (14), completing the system variables of the averaged model (11). Fig. 5 corresponds to the dashed loop in the shaded region of the generic block diagram in Fig. 3. Connection of the controller to the solid loop in the nonshaded region of Fig. 3 paves the way for a practical application. This is discussed in the next section.

Note that the example has been chosen for reasons of simplicity. Following the procedure above for unbalanced grid conditions would require the following modifications which are just sketched briefly. The averaged model (9) already considers a negative sequence for the grid voltage and current. For identifying stationary operating regimes, (13a) and (13b) no longer hold. Depending on the stationary solution of (11), the components in Table II change and the additional components $\underline{E}_{s0}^{[2]}$, $\underline{E}_{d0}^{[1]}$, $\underline{E}_{s}^{[-4]}$, $\underline{E}_{s}^{[2]}$, $\underline{E}_{d}^{[-1]}$, and $\underline{E}_{d}^{[3]}$ may appear. For the control input assignments, the presence of $\underline{V}_{y}^{[-1]}$ opens up more choices as one can see from (9). Revisiting [21], [22], and [54] allows to verify that some of them have already been proposed which links the method to the literature.

VI. Implementation

A. Translation of the System Variables

The implementation of the controller shown in Fig. 4 relies on the averaged model (11). Consequently, the interfaces consist of averaged quantities. Thus, using the same controller for the reduced system (9) or even in a practical application requires a translation of the system variables between the different contexts. While the average energy references can easily be set, the actual average energies are not directly accessible because the averaged system (11) has no real equivalent. This is why the reconstruction of the average energies requires a *forward translation* of the instantaneous energies. Here, the forward translation is implemented by subtracting the respective alternating components of the stationary solution (12) from the measured energies, leading to the approximation

$$\bar{e}_{s0} \approx e_{s0} - e_{s0,\mathrm{AC}} =: \hat{\bar{e}}_{s0} \tag{19a}$$

$$\bar{e}_{d0} \approx e_{d0} - e_{d0,\mathrm{AC}} =: \hat{\bar{e}}_{d0} \tag{19b}$$

$$\underline{\bar{e}}_{s} \approx \underline{e}_{s} - \underline{e}_{s,\mathrm{AC}} =: \underline{\hat{\bar{e}}}_{s} \tag{19c}$$

$$\underline{\bar{e}}_{d} \approx \underline{e}_{d} - \underline{e}_{d,\mathrm{AC}} =: \underline{\hat{\bar{e}}}_{d}. \tag{19d}$$

Consequently, the quantities $\hat{\bar{e}}_{s0}, \hat{\bar{e}}_{d0}, \underline{\hat{\bar{e}}}_{s}, \underline{\hat{\bar{e}}}_{d}$ will be termed *forward-translated energies* in the following. The alternating

[6] Case B in [23] offers an alternative choice where the dc current component on the ac side substitutes for the negative sequence circulating current (17d). This is not directly obvious from the averaged system (11), because the series (10) excludes a dc component on the ac side since not all applications allow it. However, after amending the series (10b) to include a dc component $\underline{I}^{[0]}$, an additional power term $V_{\mathrm{DC}}^{[0]}\underline{I}^{[0]}$ becomes available in the average energy subsystem (11d) as a control input choice.

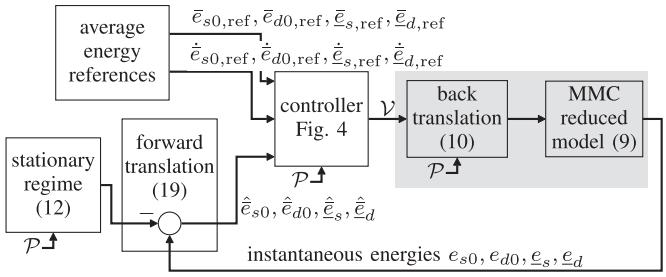

Fig. 6. Block diagram of the controller in Fig. 4 applied to the MMC reduced model (9). In case of the example from Section V-B, the shaded region is replaced by the block diagram in Fig. 7.

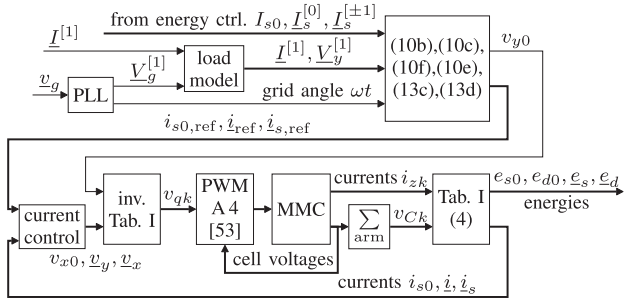

Fig. 7. Block diagram of shaded region in Fig. 6 for the example from Section V-B including current control, modulation, arm voltage equalization, and transformations as implemented on the test bench. Only the required columns from Table I or their inverse are used.

components in the forward translation (19) are calculated assuming nominal conditions, with the benefit of quick response to operating regime changes. Alternatively, moving average or low pass filtering can be used as in, e.g., [55] and [56] at the cost of an acquisition delay which is avoided by (19).

The *back translation* is implemented by the series definitions (10). The coefficients are provided by the system variables $\mathcal{V}$ and the parameters $\mathcal{P}$ of the averaged system (11).

Owing to this *forward and back translation*, the controller for the averaged system is able to control the reduced system, as shown in the block diagram in Fig. 6. Implementation of this control scheme for a practical MMC system involves replacing the reduced model (9) in Fig. 6 with the real hardware including the underlying current or voltage controllers, as required by the application. The references for these controllers are given by the series definitions (10). Some of the series (10) may already be fixed by the application, requiring their inclusion solely for modeling purposes. In such a case, only a subset of the series definitions (10) need to be implemented, reducing the computation cost.

B. Example

Except for the shaded region in Fig. 6, the other blocks remain valid for a practical implementation. For the *forward translation*, the coefficients from Table II are used. Implementing the *back translation* for the example from Section V-B to a current controlled MMC in a grid-side application merely requires the ac current (10b), the common-mode voltage (10c), the dc current (10e), and the circulating current (10f), as shown in Fig. 7. Implementation of the series (10a) and (10d) for the output voltage $\underline{v}_y$ and the dc voltage v_{DC}, respectively, is not required since the former is utilized by the ac current controller (30) and the latter is obtained via measurement. Therefore, the coefficients of the omitted series (10a) and (10d) need to be identified in order to complete the parameter set $\mathcal{P}$ since the remaining blocks may depend on it. The positive and negative sequence $\underline{V}_y^{[\pm 1]}$ can be obtained from the stationary solution of the load model (8a) after the current $\underline{i}$ and its derivative have been replaced with the help of the series (10b) and its derivative, respectively. The dc voltage $\underline{V}_{\mathrm{DC}}^{[0]}$ can directly be obtained from the measurement v_{DC}, using an optional low pass filter, if desired.

(a) (b)

Fig. 8. (a) Control cabinet and MMC cabinet. (b) Twin-cell module.

VII. Simulation and Measurement Results

The aim of this section is to illustrate some of the results from the previous sections by simulation and measurement results. A low-voltage test bench with a rapid control prototyping system and customized field-programmable gate arrays (FPGAs) is used for the experiments. The control cabinet and one MMC cabinet is shown in Fig. 8(a) and one of the twin-cell modules is shown in Fig. 8(b). In order to ease a comparison between both, for the simulation the parameters of the test bench have been used, listed in Table III.

A. Invariance of the Averaged Behavior w.r.t. the Second Harmonic of the Circulating Current

In Section V-B1 it has been stated that $\underline{I}_s^{[-2]}$ does not influence the average of the energies (as long as $\underline{V}_{y0}^{[2]} = 0$), such that its use does not affect the balancing. This is confirmed by the simulations and measurements in Figs. 9 and 10, where the complex energy reference $\underline{\bar{e}}_{d,\mathrm{ref}}$ steps from (25+j0) J to zero at $t = t_{\mathrm{step}}$ for $A = 0$ and $A = 1$, respectively. The left columns in Figs. 9 and 10 demonstrate the behavior of the translated controller (18), i.e., simulating the block diagram in Fig. 6. The corresponding measurements are shown in the right columns of each figure. In all four cases, the symmetric operation is reached after two fundamental cycles, as apparent from the equivalent cell voltages in Figs. 9(e) and 10(e), as well as from the instantaneous energies shown as solid lines in (a) to (d)

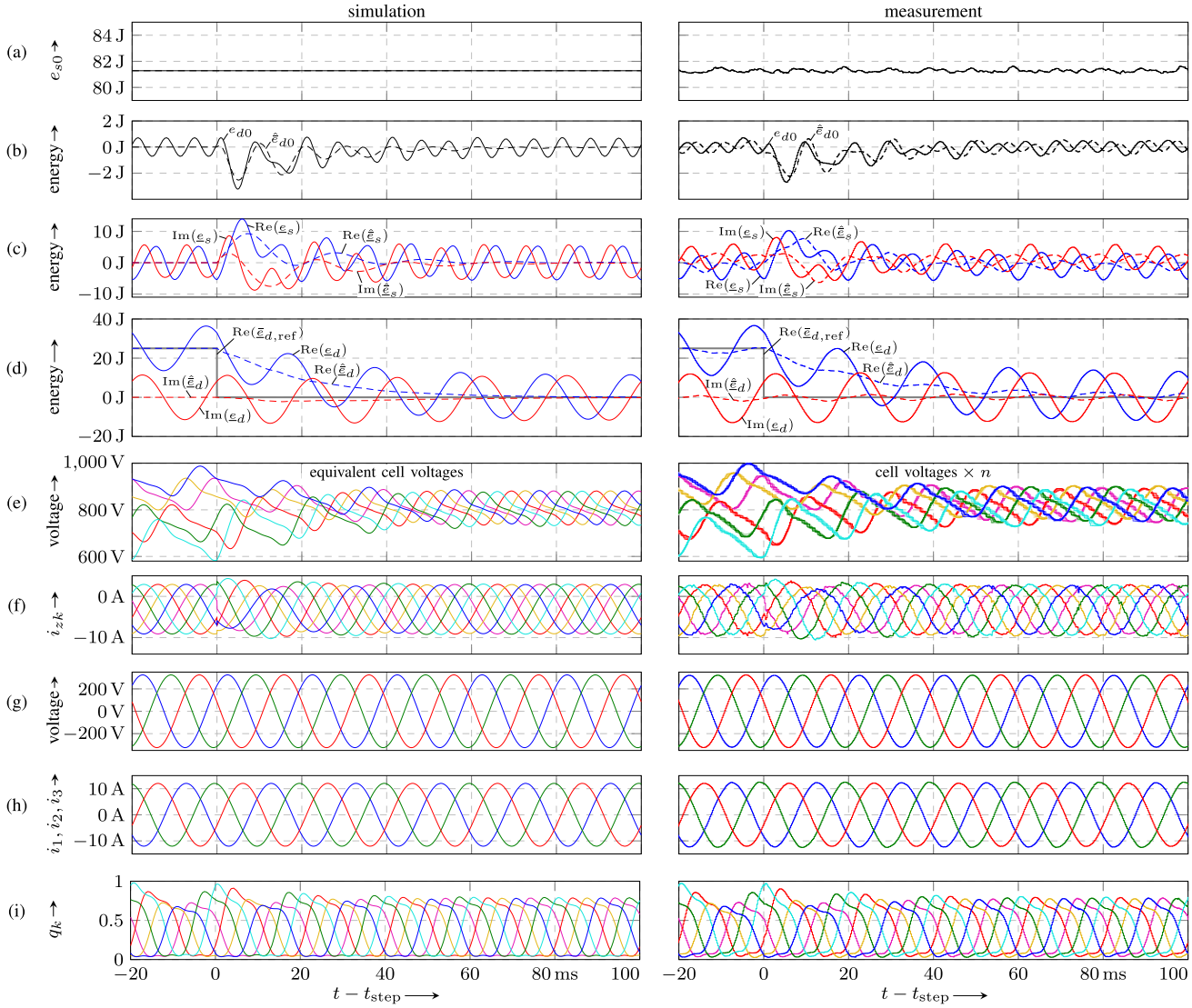

Fig. 9. Simulation (left) and measurement (right) of the regime (13) for $A = 0$ when the energy reference $\underline{\bar{e}}_{d,\mathrm{ref}}$ steps from $\underline{\bar{e}}_{d,\mathrm{ref}} = 25 + 0\mathrm{jJ}$ to zero at $t = t_{\mathrm{step}} = -2.5$ ms, i.e., symmetric operation: (a) Stored energy e_{s0} (solid), $\hat{e}_{s0}$ (dashed); (b) vertical difference e_{d0} (solid), $\hat{e}_{d0}$ (dashed); (c) complex sum $\underline{e}_s$ (solid), $\underline{\hat{e}}_s$ (dashed); (d) complex difference $\underline{e}_d$ (solid), $\underline{\hat{e}}_d$ (dashed); (e) equivalent cell voltages v_{Ck} (left), cell voltages scaled by number of cells per arm n (right); (f) arm currents i_{zk}; (g) grid voltages v_{g1}, v_{g2}, v_{g3}; (h) grid currents i_1, i_2, i_3; (i) duty-cycles q_k, $k = 1, \ldots, 6$. The instantaneous energies in (a) to (d) are drawn as solid lines, while the respective forward-translated energies are dashed. The cell voltages, arm currents, and duty-cycles on the left are calculated via the relations from Section III and on the right are measured via the real time system. Parameters are given in Table IV.

of the respective figures. The stored energy e_{s0} in all cases stays constant, because it is not coupled to the other energies and its reference is not changed. Except for a small dc and second-harmonic component in the energy $\underline{e}_s$ and a residual fundamental frequency component in the average energy $\underline{\bar{e}}_d$, the measurements in Figs. 9 and 10 show the same behavior as the simulations, respectively. Obviously, the stationary regime (12) cannot predict all details of the real energies, which explains the nonvanishing disturbances in the average energies. Most of the differences originate from additional components that were neglected in the assumptions (10) and from the nonideal behavior of the MMC, that was neglected in the modeling, e.g., semiconductor voltage drops and losses. The resemblance of the real system by the model is adequate for the purpose of control design, confirming the modeling process. Interestingly, although the instantaneous energies differ considerably between the regimes, the behavior of the forward-translated energies (19), shown as dashed lines in Figs. 9 and 10, is almost identical. This favorable feature was enabled by inclusion of the optional second-harmonic circulating current $\underline{I}_s^{[-2]}$ in the parameters $\mathcal{P}$, as discussed in Section V-B1.

B. Feedback Gain Tuning

In the context of the averaged model (11), the gains of the error dynamics (16) are not limited *a priori*. However, the validity of the averaged system (11) (and consequently that of the controller as well) is based on the assumption of slowly varying coefficients of the series (10). As shown in Section III-C, the meaning of *slowly* depends on the perturbation parameter $\varepsilon = \omega^{-1}$.

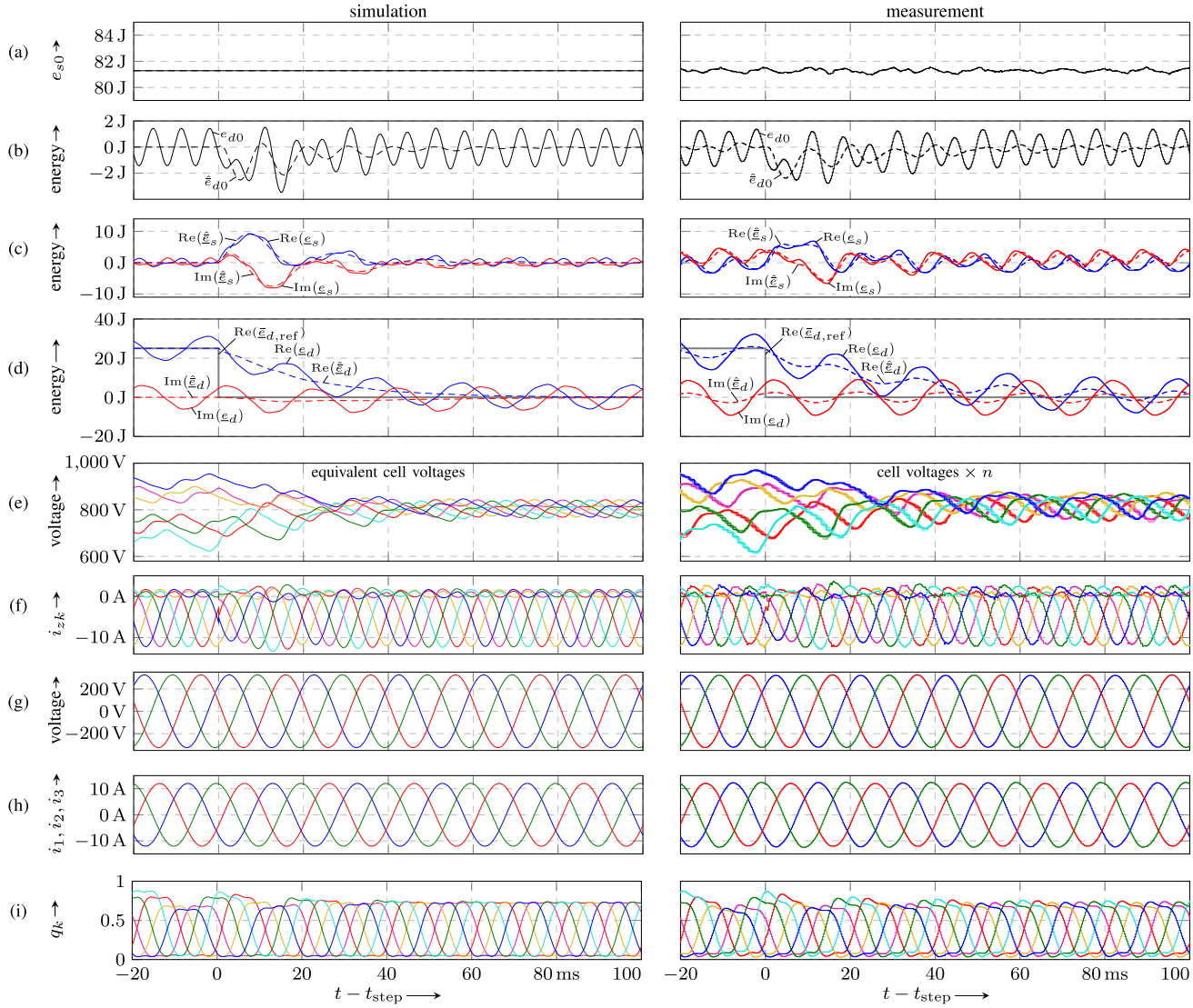

Fig. 10. Simulation (left) and measurement (right) for the same conditions as in Fig. 9 but $A = 1$.

This naturally restricts the choice of the gains, in order not to lose the ability of (16) to predict the behavior of the closed loop in Fig. 6. Note that, although a formal modeling ending up in a dynamic model as proposed here is missing in the state of the art, this gain tuning problem is equally relevant there. In either case, it comes down to a tradeoff between modeling accuracy and energy control performance.

This interesting point is investigated here by varying the gains of the error dynamics (16) in simulations and measurements. For simulation, the control schemes in Figs. 5 and 6 are considered for different gain settings during the same step change of the average energy reference $\underline{\bar{e}}_{d,\mathrm{ref}}$ as before in Figs. 9 and 10. In order to assess the energy control performance, the sum of the squared errors is used

$$K = (\bar{e}_{s0} - \bar{e}_{s0,\mathrm{ref}})^2 + (\bar{e}_{d0} - \bar{e}_{d0,\mathrm{ref}})^2 + \left|\underline{\bar{e}}_s - \underline{\bar{e}}_{s,\mathrm{ref}}\right|^2 + \left|\underline{\bar{e}}_d - \underline{\bar{e}}_{d,\mathrm{ref}}\right|^2 \tag{20}$$

for the loop in Fig. 5 and

$$\hat{K} = (\hat{\bar{e}}_{s0} - \bar{e}_{s0,\mathrm{ref}})^2 + (\hat{\bar{e}}_{d0} - \bar{e}_{d0,\mathrm{ref}})^2 + \left|\underline{\hat{\bar{e}}}_s - \underline{\bar{e}}_{s,\mathrm{ref}}\right|^2 + \left|\underline{\hat{\bar{e}}}_d - \underline{\bar{e}}_{d,\mathrm{ref}}\right|^2 \tag{21}$$

for the loop in Fig. 6, respectively. Fig. 11 shows the simulation results on the left and the measurement results on the right for the three gain settings A, B, and C, as given in Table IV.

Only the results for the complex energy $\underline{e}_d$ are shown in Fig. 11(a) and (b), because the cost functions K and $\hat{K}$ in Fig. 11(c) include all energies. With a low gain setting, the averaged system and the reduced system behave very similar, as evident from the small difference between the solid and dashed lines for case A in Fig. 11, supporting the use of the simpler loop in Fig. 5 [using the averaged model (11)] as a model for the more complicated loop in Fig. 6 [using the reduced model (5)]. With increasing gains, the difference between both systems becomes larger, as evident for the cases B and C. Gain setting B is

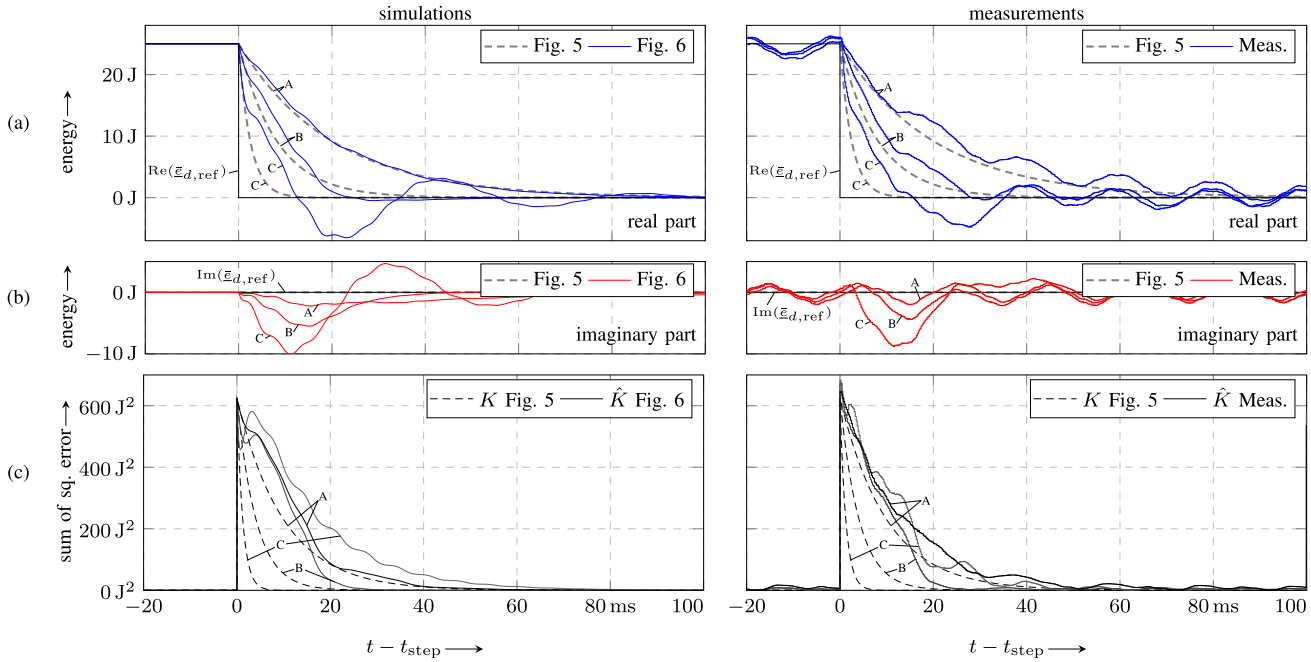

Fig. 11. Simulations (left) and measurements (right) for gain settings A, B, and C, when the energy reference $\underline{\bar{e}}_{d,\mathrm{ref}}$ is changed from $\underline{\bar{e}}_{d,\mathrm{ref}} = (25 + \mathrm{j}0)$ J to zero at $t = t_{\mathrm{step}} = -2.5$ ms: (a) Real part (b) imaginary part of the forward-translated energy $\underline{\hat{\bar{e}}}_d$ (solid) and its prediction $\underline{\bar{e}}_d$ (dashed) according to Fig. 5; (c) sum of squared errors K and $\hat{K}$, as defined in (20) and (21), respectively.

preferable over A because it offers a faster decay of $\hat{K}$, even with the larger modeling error of the averaged system, i.e., a mismatch between $\hat{K}$ and K. The setting C has no practical merit, because the sum of the squared errors $\hat{K}$ decays slower than in any of the other two cases, although it has the highest gains.

The step change from the simulations on the left in Fig. 11 was measured on a low-voltage test bench, leading to the experimental results on the right. For convenience, the corresponding solution of the loop in Fig. 5 is plotted as well using dashed lines, facilitating easy comparison with the simulation results. Despite a nonzero fundamental frequency component in the average energy $\bar{e}_d$, the measurements on the right in Fig. 11(a) and (b) show the same behavior as the simulations on the left. The additional fundamental component mainly originates from the assumption of ideal MMC behavior in the average energy approximation (19). However, these modeling inaccuracies can be accepted because the energy errors are dominated by the energy imbalance. The measurements on the right in Fig. 11(c) exhibit the same relations of the sum of squared errors (solid) to the predicted behavior (dashed) as the simulations on the left. Although the decay of the sum of the squared errors $\hat{K}$ is faster in the measurement than in the simulation, case C is still no reasonable setting for the gains since the other cases provide faster decays with lower gains.

To sum up, the growing mismatch between the average system prediction and the actual behavior indicates that it cannot be used to approximate the full system in case of increased gains. In other words, the assumption of constant coefficients of the series (10) cedes to be useful, when the specified error dynamics (16) is intended to decay too quickly. Fig. 12 illustrates this tradeoff

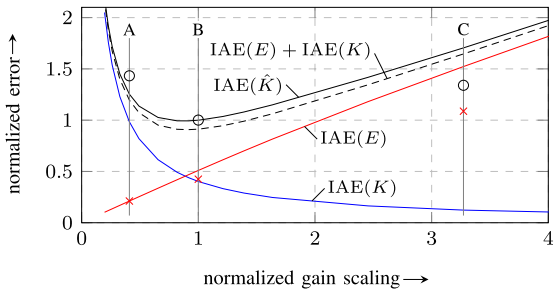

Fig. 12. $\mathrm{IAE}(\hat{K})$ of the loop in Fig. 6 (black), predicted $\mathrm{IAE}(K)$ according to the loop in Fig. 5 (blue), and the the modeling $\mathrm{IAE}(E)$ of the latter (red) for different gain settings. Solid and dashed lines indicate simulation results and the circles and cross marks indicate measurement results.

between model accuracy and controller performance by showing the integral absolute error (IAE), defined as

$$\mathrm{IAE}(x) = \int_0^\infty |x(t)| \mathrm{d}t \tag{22}$$

of both, the loop in Fig. 5, where $x = \hat{K}$ [i.e., the error dynamics (16)] and the loop in Fig. 6, where $x = K$. In order to evaluate the difference between both models, the mismatching measure $\mathrm{IAE}(E)$, with

$$E = (\hat{\bar{e}}_{s0} - \bar{e}_{s0})^2 + (\hat{\bar{e}}_{d0} - \bar{e}_{d0})^2 + \left|\underline{\hat{\bar{e}}}_s - \underline{\bar{e}}_s\right|^2 + \left|\underline{\hat{\bar{e}}}_d - \underline{\bar{e}}_d\right|^2 \tag{23}$$

is depicted as well. Application of the Integral Absolute Error (IAE) in (22) to the squared cost functions in (20), (21), and (23), effectively provides the integral square error of the loops and

of the modeling mismatch. With increasing gains, the control performance of the simplified system increases which is indicated by a decrease of $\mathrm{IAE}(K)$ while the modeling mismatch assessed by $\mathrm{IAE}(E)$ increases. Interestingly, the $\mathrm{IAE}(\hat{K})$ of the actual system features a minimum, located near the crossing of $\mathrm{IAE}(K)$ and $\mathrm{IAE}(E)$ which is why setting B is preferred, due to its vicinity to the minimum.

The measurement results from the experiments on the right in Fig. 11 are indicated in Fig. 12 by circles for $\mathrm{IAE}(\hat{K})$ and cross marks for the modeling mismatch $\mathrm{IAE}(E)$. Except for case C, i.e., the high-gain setting, the simulations agree with the measurements.

The simulation and measurement results demonstrate that the modeling mismatch $\mathrm{IAE}(E)$ is dominated by the additional cross coupling of the *back translation* which is already included in the loop in Fig. 6 and that the additional errors of a practical implementation are negligible in the context of the energy balancing.

In the case at hand, the stored energy is not relevant for this tradeoff, because the series calculation in Fig. 6 [i.e., the translated control law (18)] does not introduce any cross coupling between e_{s0} and the other energies. Consequently, the gain l_{s0} is limited by other effects, such as the underlying dc current control performance.

C. Improved Control Mapping Avoiding the Singularity in (18)

As mentioned above, the controller (18) suffers from a singularity in case $\underline{V}_y^{[1]} = 0$. As a consequence, the currents required for symmetrizing the energies may become too large if $|\underline{V}_y^{[1]}|$ is low. In such a case, e.g., during a fault ride through (FRT) condition it may be advisable to choose other inputs. As a benefit of the modeling, this is easily possible by simply following the three-step instructions given in Section V-A for this particular case. The singularity can be avoided by not already fixing $\underline{I}_s^{[\pm 3]}$ in the step *Collection of System Variables* which means assigning them the role of system variables instead of parameters. With $\underline{I}_s^{[\pm 3]}$ being now members of $\mathcal{V}$, this freedom can be exploited in the step *control input assignment* by extending the choice (17) as

$$\underline{I}_{s0}^{[\pm 3]} = \lambda_1 u_2 \mathrm{e}^{\mathrm{j}\arg(\underline{V}_{y0}^{[\pm 3]})} \tag{24a}$$

$$\underline{I}_{s}^{[\pm 3]} = \lambda_2 (u_5 - \mathrm{j}u_6) \mathrm{e}^{\mathrm{j}\arg(\underline{V}_{y0}^{[\pm 3]})} \tag{24b}$$

with the constant design parameters $\lambda_1, \lambda_2 \geq 0$. For u_1, u_3, and u_4 this leads to no changes but (18b), (18d) are replaced by

$$u_2 = \frac{-1}{|\underline{V}_y^{[1]}| + 4\lambda_1 |\underline{V}_{y0}^{[3]}|} \left(\tfrac{\mathrm{d}}{\mathrm{d}t} \bar{e}_{d0,\mathrm{ref}} - l_{d0}(\bar{e}_{d0} - \bar{e}_{d0,\mathrm{ref}}) \right) \tag{25a}$$

$$u_5 + \mathrm{j}u_6 = \frac{-1}{|\underline{V}_y^{[1]}| + 4\lambda_2 |\underline{V}_{y0}^{[3]}|} \left(\tfrac{\mathrm{d}}{\mathrm{d}t} \underline{\bar{e}}_{d,\mathrm{ref}}^{*} - l_d(\underline{\bar{e}}_{d}^{*} - \underline{\bar{e}}_{d,\mathrm{ref}}^{*}) \right). \tag{25b}$$

This means that the alternative choice of the mappings (14) avoids the singularity but leaves the error dynamics (16) of the average energies unaffected. The alternative control mapping (25) reduces to the first controller (18) by setting $\lambda_1, \lambda_2 = 0$ which is later used for easy comparison. With $\lambda_1, \lambda_2 > 0$ the controller facilitates the third harmonic in the common-mode voltage to generate additional balancing power by injecting suitable third-harmonic components in the dc current and the circulating current, respectively. In a very similar way, the common-mode voltage plays an essential role in the balancing scheme in applications with low output frequencies, e.g., in [57]–[59]. However, the model-based approach from this article allows convenient partition of the control effort during the *Control Input Assignment* and inherently provides the required phase alignment in the solution. Although a third harmonic in the circulating currents does not seem to be problematic for most applications, the feasibility of a third harmonic in the dc current may depend on the application. Here, a dc capacitor is present which can provide for this current. As long as the current is small enough not to have a significant impact on the dc voltage this will not require to take more measures.

In order to compare the behavior of both mappings, an experiment is performed, in which a three phase voltage sag with 25% remaining voltage is assumed to approach the singularity. Fig. 13 shows the measurement results during the voltage sag for the first control mapping on the left and the second control mapping on the right, i.e., for $\lambda_1, \lambda_2 = 0$ and $\lambda_1, \lambda_2 = 1$. The MMC grid current is controlled to follow common FRT requirements, i.e., during the low-voltage condition, the grid currents supply inductive apparent power to the grid as visible in Fig. 13(h). The common-mode voltage is increased during FRT to reduce the control effort of the second mapping as visible from the denominator in (25). When $\lambda_1, \lambda_2 = 0$, the increased common-mode voltage does not affect the controller, because it is properly provided for in the coefficients in Table II. The stored energy reference $\bar{e}_{s0,\mathrm{ref}}$ is increased after detection of the low-voltage condition in order to avoid saturation of the duty-cycles on the upper limit in case of the first mapping. An increase of 15 J is required to maintain a similar control margin as during the undisturbed condition, as visible in Fig. 13(i) on the left at around 7 ms. Note that this increase is not necessary for the second control mapping. It is done there just to facilitate the comparison.

The nominal average behavior of both cases is identical, because they have identical error dynamics (16) as visible from the calculated average energies depicted by dotted lines in Fig. 13(a)–(d). The dotted lines have been simulated with the loop in Fig. 5 using the step change from the experiments. Compared to all other energy variables, the stored energy $\bar{e}_{s0}$ has a quicker response due to a higher proportional gain and a small overshoot due to the additional integral part.

The behavior of the forward-translated energies differs noticeably between both cases, as visible from the dashed lines. Most notably, this concerns the complex energy sum $\hat{\underline{\bar{e}}}_s$ as visible in Fig. 13(c). The sudden increase of the imaginary part in the left diagram reveals an undesired impact originating from a disproportionately high-negative sequence circulating current $\underline{I}_s^{[-1]}$ emitted by the controller (18d) for $\underline{\bar{e}}_d$ as anticipated near the singularity at $|\underline{V}_y^{[1]}| = 0$. Thus, $\underline{I}_s^{[-1]}$ violates the assumption of changing slowly in time. Consequently, this impact cannot be explained by the averaged system since $\underline{I}_s^{[-1]}$ does not appear on the right-hand side of (11d). However, (5d) is still able to explain the observed coupling.

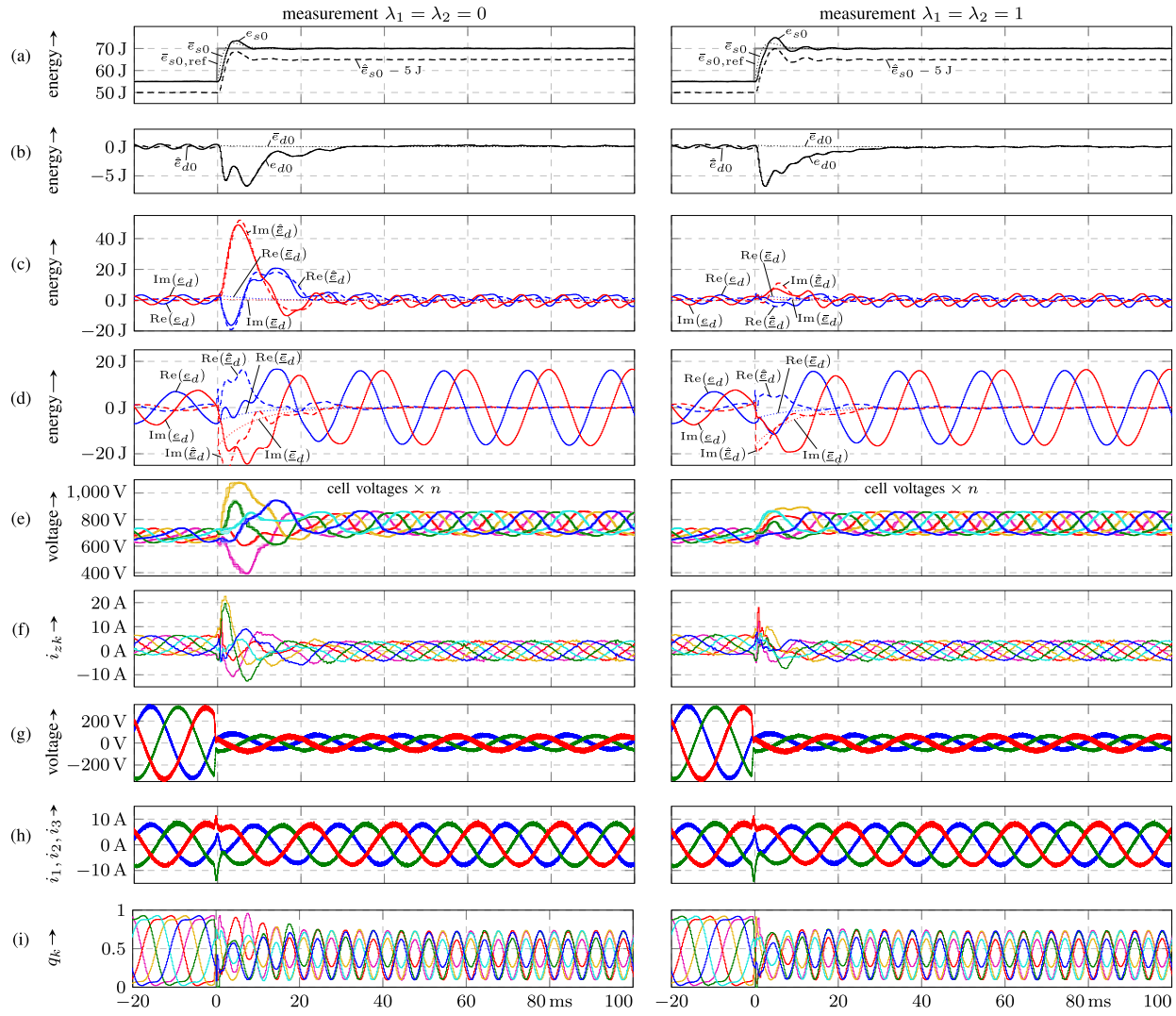

Fig. 13. Measurements for $\lambda_1 = \lambda_2 = 0$ (left) and $\lambda_1 = \lambda_2 = 1$ (right) during a three phase grid voltage sag: (a) Stored energy e_{s0} (solid), $\hat{\bar{e}}_{s0}$ (dashed), $\bar{e}_{s0}$ (dotted); (b) vertical difference e_{d0} (solid), $\hat{\bar{e}}_{d0}$ (dashed), $\bar{e}_{d0}$ (dotted); (c) complex sum $\underline{e}_s$ (solid), $\hat{\underline{\bar{e}}}_s$ (dashed), $\underline{\bar{e}}_s$ (dotted); (d) complex difference $\underline{e}_d$ (solid), $\hat{\underline{\bar{e}}}_d$ (dashed), $\underline{\bar{e}}_d$ (dotted); (e) cell voltages scaled by number of cells per arm n; (f) arm currents i_{zk}; (g) grid voltages v_{g1}, v_{g2}, v_{g3}; (h) grid currents i_1, i_2, i_3; (i) duty-cycles q_k, $k = 1, \ldots, 6$. Measured variables in (a)–(f), (i) have been taken from the control system. Traces in (g), (h) have been taken via voltage and current probes connected to an oscilloscope. The dotted lines have been calculated with the loop in Fig. 5. At $t = 0$ ms the control system detects the low-voltage condition.

Comparing the arm currents and cell voltages for both cases, one can see that the alternative mapping leads to a better balancing result with even lower arm currents than the original one.

As visible from the model (9), the energies e_{s0}, e_{d0}, and $\underline{e}_d$ are coupled via the current i_{s0}. For both control mappings, an error in e_{s0} has a backlash on the other two. But for the first mapping, it is not the other way around. This is only introduced by the second one because it relies on the third harmonic of the dc current. This can be seen in Fig. 13(a) by comparing left to right: The oscillation in e_{s0} is an image of the error in e_{d0}. In view of the improved control performance, the additional coupling of the second mapping can easily be accepted.

During asymmetric faults, a negative sequence of the grid voltage can appear, which was assumed to be zero in the example regime (13). A small amplitude of the negative sequence, i.e., $|\underline{V}_y^{[-1]}| \ll |\underline{V}_y^{[1]}|$, will act as a disturbance. Nonetheless, the controller can be expected to reach the desired operating regime reasonably well. However, as an advantage of the method, it allows to account for a nonzero $\underline{V}_y^{[-1]}$ already in the controller design, as outlined at the end of Section V.

VIII. Conclusion

The balancing control of MMCs is challenging because for most practical applications the system is underactuated. However, for many applications a separation of timescales can be observed that allows to solve the balancing problem by employing characteristic harmonics of some system variables as inputs. Although widely used in the literature, a proof of this concept was missing. The present article closes this gap by proposing a suitable modeling framework. Starting from the MMCs circuit equations, two methods of singular perturbation theory result in a

simplified dynamic model describing the behavior of the average of the system variables. This modeling provides sufficiently actuated systems, well suited for a model-based controller design, because a controller can easily be obtained from a desired error dynamics. Moreover, the simplified model has been used to identify and describe stationary operating regimes. In order to ease the understanding, the findings are illustrated by examples that rely on well-known operating regimes. Since the design procedure reveals a singularity in one of the established control methods, it is used to obtain a control law avoiding this problem.

Nevertheless, the framework has some limitations: As any model-based scheme, it is potentially susceptible to unmodeled phenomena and relies on the knowledge of system parameters. The assumptions regarding the Fourier and Taylor series are essential for the modeling which means that the coefficients of the Fourier series may only change slowly in time. Ignoring this would impair the forward translation and may lead to an undesired control performance. Thus, model accuracy and balancing performance are conflicting objectives and a tradeoff needs to be found. Although often not mentioned explicitly, this problem applies to any similar balancing schemes. This is why, this tradeoff situation is investigated in detail in order to find a compromise between both objectives. Simulation studies and experimental results for a low-voltage test bench support the results and one may expect that these are transferable to industrial medium and high-voltage applications as well.

The present article focuses on the method with some illustrative examples. A detailed discussion of other relevant cases, e.g., unbalanced grid voltages or the startup of an ac motor, will be subject of further research.

APPENDIX

A. Systems in Standard Form

According to [60], systems in the so-called standard form can be split into a slow and a fast subsystem which can to some extent be considered as independent from each other. The standard form reads

$$\varepsilon \dot{z}_f = f_f(z_f, z_s, \varepsilon) \tag{26a}$$

$$\dot{z}_s = f_s(z_f, z_s, \varepsilon) \tag{26b}$$

where $z_f \in \mathbb{R}^{n_f}$ and $z_s \in \mathbb{R}^{n_s}$ contain the variables attributed to the fast and slow time scale, respectively. The perturbation parameter $0 < \varepsilon \ll 1$ is considered to be small, which allows to separate the fast dynamics from the slow dynamics simply by setting $\varepsilon = 0$. Functions $\phi(z_s)$ fulfilling

$$0 = f_f(\phi(z_s), z_s, 0) \tag{27}$$

constitute quasi-stationary solutions for the trajectories z_f. If the eigenvalues of $\partial f_f / \partial z_f$ all have a real part smaller than a fixed negative number, these solutions are considered to be attractive and will be reached quickly in the context of time t. Thus, for the slow dynamics

$$\dot{z}_s = f_s(\phi(z_s), z_s, 0) \tag{28}$$

is usually a good approximation which implies that z_f assumes $\phi(z_s)$ immediately.

B. Application to the MMC Model

Separation of time scales is often done implicitly without investigating to which extent this simplification is justified. Fortunately, the method briefly recalled above gives a framework which allows to quantify this by examining the perturbation parameter ε. Examples for the use of this method in the field of power electronics can be found in [61], [62], or in [63] even for an MMC but more from the power systems perspective.

The models (5)–(8) still do not have enough information on the dynamics of the currents because the inputs are not fixed yet. Thus, it is necessary to design current controllers for instance by specifying the error dynamics

$$\tfrac{\mathrm{d}}{\mathrm{d}t}(i_{s0} - i_{s0,d}) = -k_{s0}(i_{s0} - i_{s0,d}) \tag{29a}$$

$$\tfrac{\mathrm{d}}{\mathrm{d}t}(\underline{i}_s - \underline{i}_{s,d}) = -k_s(\underline{i}_s - \underline{i}_{s,d}) \tag{29b}$$

$$\tfrac{\mathrm{d}}{\mathrm{d}t}(\underline{i} - \underline{i}_d) = -k_d(\underline{i} - \underline{i}_d) \tag{29c}$$

where $i_{s0,d}, \underline{i}_{s,d}, \underline{i}_d$ denote the reference trajectories. Using (7a), (7b), and (8a), and solving for v_{x0}, $\underline{v}_x$ and $\underline{v}_y$ yields the control law. In case of the latter, this leads to

$$\underline{v}_y = L\tfrac{\mathrm{d}}{\mathrm{d}t}\underline{i}_d + \underline{v}_g + R\underline{i} - Lk_d(\underline{i} - \underline{i}_d). \tag{30}$$

The system constituted now by (5a)–(5d) and (29) can be brought in the form (26) by applying an appropriate scaling [60]:

$$x = \tilde{x} C v_{\mathrm{DC}}^2, \quad (x, \tilde{x}) \in \{(e_{s0}, \tilde{e}_{s0}), (e_{d0}, \tilde{e}_{d0}) \; (\underline{e}_s, \underline{\tilde{e}}_s), (\underline{e}_d, \underline{\tilde{e}}_d)\} \tag{31a}$$

$$x = \tilde{x}\hat{I}, (x, \tilde{x}) \in \{(i_{s0}, \tilde{i}_{s0}), (\underline{i}, \underline{\tilde{i}}), (\underline{i}_s, \underline{\tilde{i}}_s)\} \tag{31b}$$

$$x = \tilde{x} v_{\mathrm{DC}}, (x, \tilde{x}) \in \{(v_{y0}, \tilde{v}_{y0}), (\underline{v}_y, \underline{\tilde{v}}_y), (\underline{v}_{y\Delta}, \underline{\tilde{v}}_{y\Delta})\} \tag{31c}$$

$$x = \tilde{x}/\tau_1, (x, \tilde{x}) \in \{(k_{s0}, \tilde{k}_{s0}), (k_s, \tilde{k}_s), (k_d, \tilde{k}_d)\} \tag{31d}$$

$$t = \tilde{t}\tau_2 \tag{31e}$$

with $\tau_1 = \frac{(L_z + M_z)\hat{I}}{v_{\mathrm{DC}}}$, $\tau_2 = \frac{C v_{\mathrm{DC}}}{\hat{I}}$, and $\hat{I}$ being the rated arm current peak value.

Applying this change of coordinates, the model assumes the form (26) as can be seen from

$$\tfrac{\mathrm{d}}{\mathrm{d}\tilde{t}}\tilde{e}_{s0} = \tilde{i}_{s0} - \mathrm{Re}\big(\underline{\tilde{i}}\underline{\tilde{v}}_y^*\big) \tag{32a}$$

$$\tfrac{\mathrm{d}}{\mathrm{d}\tilde{t}}\tilde{e}_{d0} = -2\tilde{v}_{y0}\tilde{i}_{s0} - \mathrm{Re}\Big(\underline{\tilde{i}}_s^*\underline{\tilde{v}}_y\Big) \tag{32b}$$

$$\tfrac{\mathrm{d}}{\mathrm{d}\tilde{t}}\underline{\tilde{e}}_s = \underline{\tilde{i}}_s - \underline{\tilde{v}}_y^*\tilde{i}^* - 2\underline{\tilde{i}}\tilde{v}_{y0} \tag{32c}$$

$$\tfrac{\mathrm{d}}{\mathrm{d}\tilde{t}}\underline{\tilde{e}}_d = \underline{\tilde{i}} - \underline{\tilde{v}}_{y\Delta}^*\tilde{i}_s^* - 2\underline{\tilde{i}}_s\tilde{v}_{y0} - 2\tilde{i}_{s0}\underline{\tilde{v}}_{y\Delta} \tag{32d}$$

$$\varepsilon\tfrac{\mathrm{d}}{\mathrm{d}\tilde{t}}(\tilde{i}_{s0} - \tilde{i}_{s0,d}) = -\tilde{k}_{s0}(\tilde{i}_{s0} - \tilde{i}_{s0,d}) \tag{32e}$$

$$\varepsilon\tfrac{\mathrm{d}}{\mathrm{d}\tilde{t}}(\underline{\tilde{i}}_s - \underline{\tilde{i}}_{s,d}) = -\tilde{k}_s(\underline{\tilde{i}}_s - \underline{\tilde{i}}_{s,d}) \tag{32f}$$

$$\varepsilon\tfrac{\mathrm{d}}{\mathrm{d}\tilde{t}}(\underline{\tilde{i}} - \underline{\tilde{i}}_d) = -\tilde{k}_d(\underline{\tilde{i}} - \underline{\tilde{i}}_d) \tag{32g}$$

with

$$\tilde{\underline{v}}_{y\Delta} = \tilde{\underline{v}}_y - \frac{M_z}{L_z + M_z}\varepsilon \frac{\mathrm{d}}{\mathrm{d}\tilde{t}}\tilde{\underline{i}} \tag{33a}$$

$$\tilde{\underline{v}}_y = \frac{\hat{I}^2}{C v_{\mathrm{DC}}^2} L \frac{\mathrm{d}}{\mathrm{d}\tilde{t}}\tilde{\underline{i}}_d + \tilde{\underline{v}}_g + R\frac{\hat{I}}{v_{\mathrm{DC}}}\tilde{\underline{i}} - \frac{L}{L_z + M_z}\tilde{k}_d(\tilde{\underline{i}} - \tilde{\underline{i}}_d). \tag{33b}$$

The perturbation parameter $\varepsilon = \frac{\tau_1}{\tau_2} = \frac{(L_z+M_z)\hat{I}^2}{C v_{\mathrm{DC}}^2}$ can be interpreted as the ratio between the energy stored in the inductors of one phase if the arm current has its maximum possible value and the energy stored in the capacitors of this phase if the voltage of the equivalent cells is v_{DC}. Thus, in a practical application it will hold $0 < \varepsilon \ll 1$ and $\varepsilon \ll \tilde{k}_{s0}, \tilde{k}_s, \tilde{k}_d$ which enables a separation of the timescales.

Following the brief introduction of the method from Appendix A, a reduced model can be obtained by setting $\varepsilon = 0$ which yields the following quasi-stationary solutions:

$$\tilde{i}_{s0} = \tilde{i}_{s0,d} \tag{34a}$$

$$\tilde{\underline{i}}_s = \tilde{\underline{i}}_{s,d} \tag{34b}$$

$$\tilde{\underline{i}} = \tilde{\underline{i}}_d \tag{34c}$$

$$\tilde{\underline{v}}_{y\Delta} = \tilde{\underline{v}}_y \tag{34d}$$

$$\tilde{\underline{v}}_y = \frac{\hat{I}^2}{C v_{\mathrm{DC}}^2} L \frac{\mathrm{d}}{\mathrm{d}\tilde{t}}\tilde{\underline{i}}_d + \tilde{\underline{v}}_g + R\frac{\hat{I}}{v_{\mathrm{DC}}}\tilde{\underline{i}}_d \tag{34e}$$

if one assumes $\frac{L_z+M_z}{M_z} \gg \varepsilon$. This means an approximation of the original system is now given by (32a)–(32d) and (34). Rolling back the scaling leads to (9) in Section III-B.

In order to check whether the conditions above are fulfilled for the test bench used, the time constants and the perturbation parameter can be calculated using the parameters from Table III and $v_{\mathrm{DC}} = V_{\mathrm{DC,r}}$ as $\tau_1 = 82\mu\mathrm{s}$, $\tau_2 = 1.6\mathrm{ms}$, and $\varepsilon = \tau_1/\tau_2 = 0.051 \ll 1$. The normalized controller gains for the laboratory MMC are set to reduce the control error by 97% within one sampling time step yielding $\tilde{k}_d, \tilde{k}_s, \tilde{k}_{s0} = 0.4 \gg \varepsilon$. Thus, the conditions can be considered to be fulfilled.

REFERENCES

[1] R. Marquardt, A. Lesnicar, and J. Hildinger, "Modulares Stromrichterkonzept für Netzkupplungsanwendungen bei hohen Spannungen," in *Proc. ETG-Fachtagung*, Bad Nauheim, Germany, Apr. 2002.

[2] A. Lesnicar and R. Marquardt, "A new modular voltage source inverter topology," in *Proc. Eur. Conf. Power Electron. Appl.*, Toulouse, France, Sep. 2003.

[3] J. Kolb, F. Kammerer, and M. Braun, "A novel control scheme for low frequency operation of the modular multilevel converter," in *Proc. Int. Exhib. Conf. Power Electron., Intell. Motion, Renewable Energy Energy Manage. Eur.*, Nuremberg, Germany, May 2011.

[4] M. Schröder, S. Henninger, J. Jäger, A. Rašić, H. Rubenbauer, and T. Lang, "An enhanced modulator concept for the modular multilevel converter," in *Proc. 16th Eur. Conf. Power Electron. Appl.*, Lappeenranta, Finland, Aug. 2014.

[5] D. Siemaszko, "Fast sorting method for balancing capacitor voltages in modular multilevel converters," *IEEE Trans. Power Electron.*, vol. 30, no. 1, pp. 463–470, Jan. 2015.

[6] V. Hofmann and M.-M. Bakran, "A capacitor voltage balancing algorithm for hybrid modular multilevel converters in HVDC applications," in *Proc. 12th Int. Conf. Power Electron. Drive Syst.*, Honolulu, Hawaii, USA, Dec. 2017, pp. 691–696.

[7] A. Pérez-Basante, S. Ceballos, G. Konstantinou, M. Liserre, J. Pou, and I. M. de Alegría, "Circulating current control for modular multilevel converter based on selective harmonic elimination with ultra-low switching frequency," in *Proc. 18th Eur. Conf. Power Electron. Appl.*., Karlsruhe, Germany, Sep. 2016.

[8] F. Hahn, M. Andresen, G. Buticchi, and M. Liserre, "Thermal analysis and balancing for modular multilevel converters in HVDC applications," *IEEE Trans. Power Electron.*, vol. 33, no. 3, pp. 1985–1996, Mar. 2018.

[9] S. Fuchs, S. Beck, and J. Biela, "Analysis and reduction of the output voltage error of PWM for modular multilevel converters," *IEEE Trans. Ind. Electron.*, vol. 66, no. 3, pp. 2291–2301, Mar. 2019.

[10] L. Harnefors, A. Antonopoulos, S. Norrga, L. Ängquist, and H.-P. Nee, "Dynamic analysis of modular multilevel converters," *IEEE Trans. Ind. Electron.*, vol. 60, no. 7, pp. 2526–2537, Jul. 2013.

[11] S. Debnath, J. Qin, B. Bahrani, M. Saeedifard, and P. Barbosa, "Operation, control, and applications of the modular multilevel converter: A review," *IEEE Trans. Power Electron.*, vol. 30, no. 1, pp. 37–53, Jan. 2015.

[12] A. Antonopoulos, L. Ängquist, L. Harnefors, K. Ilves, and H.-P. Nee, "Global asymptotic stability of modular multilevel converters," *IEEE Trans. Ind. Electron.*, vol. 61, no. 2, pp. 603–612, Feb. 2014.

[13] W. van der Merwe, P. Hokayem, and L. Stepanova, "Analysis of the n-cell single phase MMC natural balancing mechanism," *IEEE J. Emerg. Sel. Topics Power Electron.*, vol. 2, no. 4, pp. 1149–1158, Dec. 2014.

[14] B. P. McGrath, C. A. Teixeira, and D. G. Holmes, "Optimized phase disposition (PD) modulation of a modular multilevel converter," *IEEE Trans. Ind. Appl.*, vol. 53, no. 5, pp. 4624–4633, Sep. 2017.

[15] E. Sánchez-Sánchez, E. Prieto-Araujo, A. Junyent-Ferré, and O. Gomis-Bellmunt, "Analysis of MMC energy-based control structures for VSC-HVDC links," *IEEE J. Emerg. Sel. Topics Power Electron.*, vol. 6, no. 3, pp. 1065–1076, Sep. 2018.

[16] E. P. Araujo, A. Junyent-Ferré, C. Collados-Rodríguez, G. Clariana-Colet, and O. Gomis-Bellmunt, "Control design of modular multilevel converters in normal and AC fault conditions for HVDC grids," *Electric Power Syst. Res.*, vol. 152, pp. 424–437, Nov. 2017.

[17] H. Bärnklau, A. Gensior, and J. Rudolph, "A model-based control scheme for modular multilevel converters," *IEEE Trans. Ind. Electron.*, vol. 60, no. 12, pp. 5359–5375, Dec. 2013.

[18] H. Fehr, A. Gensior, and M. Müller, "Analysis and trajectory tracking control of a modular multilevel converter," *IEEE Trans. Power Electron.*, vol. 30, no. 1, pp. 398–407, Jan. 2015.

[19] H. Fehr and A. Gensior, "Improved energy balancing of grid-side modular multilevel converters by optimized feedforward circulating currents and common-mode voltage," *IEEE Trans. Power Electron.*, vol. 33, no. 12, pp. 10 903–10 913, Dec. 2018.

[20] J. Kolb, F. Kammerer, M. Gommeringer, and M. Braun, "Cascaded control system of the modular multilevel converter for feeding variable-speed drives," *IEEE Trans. Power Electron.*, vol. 30, no. 1, pp. 349–357, Jan. 2015.

[21] M. Schröder, F. Mahr, J. Jäger, and S. Hänsel, "Energy balancing in the modular multilevel converter under unbalanced grid conditions," in *Proc. 19th Eur. Conf. Power Electron. Appl.*, Warsaw, Poland, Sep. 2017.

[22] A. Leon and S. J. Amodeo, "Energy balancing improvement of modular multilevel converters under unbalanced grid conditions," *IEEE Trans. Power Electron.*, vol. 32, no. 8, pp. 6628–6637, Aug. 2017.

[23] G. Bergna-Diaz, J. Freytes, X. Guillaud, S. D. Arco, and J. A. Suul, "Analysis of MMC dynamics in DQZ coordinates for vertical and horizontal energy balancing control," in *Proc. 44th Annu. Conf. IEEE Ind. Electron. Soc.*, Washington, DC, USA, Oct. 2018, pp. 5999–6006.

[24] M. Jankovic, A. Costabeber, A. Watson, and J. C. Clare, "Arm-balancing control and experimental validation of a grid-connected MMC with pulsed DC load," *IEEE Trans. Ind. Electron.*, vol. 64, no. 12, pp. 9180–9190, Dec. 2017.

[25] P. Himmelmann and M. Hiller, "A generalized approach to the analysis and control of modular multilevel converters," in *Proc. Int. Exhib. Conf. Power Electron., Intell. Motion, Renewable Energy Energy Manage.*, Nuremberg, Germany, May 2017.

[26] D. Karwatzki and A. Mertens, "Generalized control approach for a class of modular multilevel converter topologies," *IEEE Trans. Power Electron.*, vol. 33, no. 4, pp. 2888–2900, Apr. 2018.

[27] H. Fehr and A. Gensior, "Eigenvalue optimization of the energy balancing feedback for modular multilevel converters," *IEEE Trans. Power Electron.*, vol. 34, no. 11, pp. 11 482–11 495, Nov. 2019.

[28] G. J. Kish and P. W. Lehn, "Modeling techniques for dynamic and steady-state analysis of modular multilevel DC/DC converters," *IEEE Trans. Power Del.*, vol. 31, no. 6, pp. 2502–2510, Dec. 2016.

[29] O. C. Sakinci and J. Beerten, "Generalized dynamic phasor modeling of the MMC for small-signal stability analysis," *IEEE Trans. Power Del.*, vol. 34, no. 3, pp. 991–1000, Jun. 2019.
[30] J. Rupasinghe, S. Filizadeh, and L. Wang, "A dynamic phasor model of an MMC with extended frequency range for EMT simulations," *IEEE J. Emerg. Sel. Topics Power Electron.*, vol. 7, no. 1, pp. 30–40, Mar. 2019.
[31] Z. Xu, B. Li, S. Wang, S. Zhang, and D. Xu, "Generalized single-phase harmonic state space modeling of the modular multilevel converter with zero-sequence voltage compensation," *IEEE Trans. Ind. Electron.*, vol. 66, no. 8, pp. 6416–6426, Aug. 2019.
[32] Y. Ma, H. Lin, Z. Wang, and Z. Ze, "Stability analysis of modular multilevel converter based on harmonic state-space theory," *IET Power Electron.*, vol. 12, no. 15, pp. 3987–3997, Dec. 2019.
[33] J. Lyu, X. Zhang, X. Cai, and M. Molinas, "Harmonic state-space based small-signal impedance modeling of a modular multilevel converter with consideration of internal harmonic dynamics," *IEEE Trans. Power Electron.*, vol. 34, no. 3, pp. 2134–2148, Mar. 2019.
[34] F. Verhulst, *Nonlinear Differential Equations and Dynamical Systems*. Berlin, Germany: Springer, 2000.
[35] S. Engel and R. De Doncker, "Control of the modular multi-level converter for minimized cell capacitance," in *Proc. 14th Eur. Conf. Power Electron. Appl.*, Birmingham, U.K., Aug. 2011.
[36] M. Vasiladiotis, N. Cherix, and A. Rufer, "Accurate capacitor voltage ripple estimation and current control considerations for grid-connected modular multilevel converters," *IEEE Trans. Power Electron.*, vol. 29, no. 9, pp. 4568–4579, Sep. 2014.
[37] J. Pou, S. Ceballos, G. Konstantinou, V. Agelidis, R. Picas, and J. Zaragoza, "Circulating current injection methods based on instantaneous information for the modular multilevel converter," *IEEE Trans. Ind. Electron.*, vol. 62, no. 2, pp. 777–788, Feb. 2015.
[38] X. Li, Q. Song, W. Liu, S. Xu, Z. Zhu, and X. Li, "Performance analysis and optimization of circulating current control for modular multilevel converter," *IEEE Trans. Ind. Electron.*, vol. 63, no. 2, pp. 716–727, Feb. 2016.
[39] J. Hu, L. Lin, M. Xiang, M. Lu, J. Zhu, and Z. He, "Improved design and control of FBSM MMC with boosted AC voltage and reduced DC capacitance," *IEEE Trans. Ind. Electron.*, vol. 65, no. 3, pp. 1919–1930, Mar. 2018.
[40] J. Wang, X. Han, H. Ma, and Z. Bai, "Analysis and injection control of circulating current for modular multilevel converters," *IEEE Trans. Ind. Electron.*, vol. 66, no. 3, pp. 2280–2290, Mar. 2019.
[41] H. Khalil, *Nonlinear Systems*. 3rd ed., Englewood Cliffs, NJ, USA: Prentice Hall, 2002.
[42] H. Saad, X. Guillaud, J. Mahseredjian, S. Dennetière, and S. Nguefeu, "MMC capacitor voltage decoupling and balancing controls," *IEEE Trans. Power Del.*, vol. 30, no. 2, pp. 704–712, Apr. 2015.
[43] M. A. Pérez, S. Bernet, J. Rodríguez, S. Kouro, and R. Lizana, "Circuit topologies, modeling, control schemes, and applications of modular multilevel converters," *IEEE Trans. Power Electron.*, vol. 30, no. 1, pp. 4–17, Jan. 2015.
[44] A. Dekka, B. Wu, R. L. Fuentes, M. Perez, and N. R. Zargari, "Evolution of topologies, modeling, control schemes, and applications of modular multilevel converters," *IEEE J. Emerg. Sel. Topics Power Electron.*, vol. 5, no. 4, pp. 1631–1656, Dec. 2017.
[45] H. Bärnklau, A. Gensior, and S. Bernet, "Derivation of an equivalent submodule per arm for modular multilevel converters," in *Proc. 15th Int. Power Electron. Motion Control Conf.*, 2012.
[46] A. M. Lopez, D. E. Quevedo, R. P. Aguilera, T. Geyer, and N. Oikonomou, "Limitations and accuracy of a continuous reduced-order model for modular multilevel converters," *IEEE Trans. Power Electron.*, vol. 33, no. 7, pp. 6292–6303, Jul. 2018.
[47] H. Fehr, "Beiträge zur Modulation, Modellbildung und Energieregelung von modularen Mehrpunktstromrichtern (M2C)," (in German), Dr.-Ing. dissertation, Technische Universität Dresden, Jul. 2019.
[48] S. Fuchs, S. Beck, and J. Biela, "High output voltage precision PWM for modular multilevel converters," in *Proc. Eur. Conf. Power Electron. Appl.*, Warsaw, Poland, Sep. 2017.
[49] G. Bergna *et al.*, "A generalized power control approach in ABC frame for modular multilevel converter HVDC links based on mathematical optimization," *IEEE Trans. Power Del.*, vol. 29, no. 1, pp. 386–393, Feb. 2014.
[50] G. Bergna-Diaz, J. A. Suul, and S. D'Arco, "Energy-based state-space representation of modular multilevel converters with a constant equilibrium point in steady-state operation," *IEEE Trans. Power Electron.*, vol. 33, no. 6, pp. 4832–4851, Jun. 2018.
[51] M. Fliess, J. Lévine, P. Martin, and P. Rouchon, "Flatness and defect of nonlinear systems: introductory theory and examples," *Int. J. Control*, vol. 61, pp. 1327–1361, 1995.
[52] H. Fehr and A. Gensior, "Model-based circulating current references for MMC cell voltage ripple reduction and loss-equivalent arm current assessment," in *Proc. 21st Eur. Conf. Power Electron. Appl.*, Genoa, Italy, Sep. 2019.
[53] H. Fehr, A. Gensior, and S. Bernet, "Experimental evaluation of PWM-methods for modular multilevel converters," in *Proc. 18th Eur. Conf. Power Electron. Appl.*, Karlsruhe, Germany, Sep. 2016.
[54] E. Behrouzian and M. Bongiorno, "Investigation of negative-sequence injection capability of cascaded H-bridge converters in star and delta configuration," *IEEE Trans. Power Electron.*, vol. 32, no. 2, pp. 1675–1683, Feb. 2017.
[55] H. D. Tafti, A. I. Maswood, G. Konstantinou, C. D. Townsend, P. Acuna, and J. Pou, "Flexible control of photovoltaic grid-connected cascaded H-bridge converters during unbalanced voltage sags," *IEEE Trans. Ind. Electron.*, vol. 65, no. 8, pp. 6229–6238, Aug. 2018.
[56] J. I. Y. Ota, Y. Shibano, and H. Akagi, "Low-voltage-ride-through (LVRT) capability of a phase-shifted-PWM STATCOM using the modular multilevel cascade converter based on single-star bridge-cells (MMCC-SSBC)," in *Proc. Energy Convers. Congr. Expo.*, Denver, CO, USA, Sep. 2013, pp. 3062–3069.
[57] A. Antonopoulos, L. Ängquist, S. Norrga, K. Ilves, and H.-P. Nee, "Modular multilevel converter AC motor drives with constant torque form zero to nominal speed," in *Proc. Energy Convers. Congr. Expo.*, Raleigh, NC, USA, Sep. 2012, pp. 739–746.
[58] A. J. Korn, M. Winkelnkemper, and P. Steimer, "Low output frequency operation of the modular multi-level converter," in *Proc. Energy Convers. Congr. Expo.*, Atlanta, USA, Sep. 2010, pp. 3993–3997.
[59] P. Himmelmann, M. Hiller, D. Krug, and M. Beuermann, "A new modular multilevel converter for medium voltage high power oil and gas motor drive applications," in *Proc. 18th Eur. Conf. Power Electron. Appl.*, Karlsruhe, Germany, Sep. 2016.
[60] P. Kokotović, H. K. Khalil, and J. O'Reilly, *Singular Perturbation Methods in Control – Analysis and Design* (Classics in Applied Mathematics). Philadelphia, PA, USA: SIAM, 1999.
[61] Z. Sorchini and P. T. Krein, "Formal derivation of direct torque control for induction machines," *IEEE Trans. Power Electron.*, vol. 21, no. 5, pp. 1428–1436, Sep. 2006.
[62] J. W. Kimball and P. T. Krein, "Singular perturbation theory for DC-DC converters and application to PFC converters," *IEEE Trans. Power Electron.*, vol. 23, no. 6, pp. 2970–2981, Nov. 2008.
[63] S. Zhu *et al.*, "Reduced-order dynamic model of modular multilevel converter in long time-scale and its application in power system low-frequency oscillation analysis," *IEEE Trans. Power Del.*, vol. 34, no. 6, pp. 2110–2122, Dec. 2019.

Albrecht Gensior received the Dipl.-Ing. and Dr.-Ing. degrees in electrical engineering from Technische Universität Dresden (TU Dresden), Dresden, Germany, in 2003 and 2008, respectively.

He is currently Professur Leistungselektronik, with Elektrotechnisches Institut, TU Dresden, where he is involved in research projects dealing with the control of power electronic converters and drives. His research interests include nonlinear controller design and observers for these applications.

Hendrik Fehr received the Dipl.-Ing. and Dr.-Ing. degree in electrical engineering from Technische Universität Dresden (TU Dresden), Germany, in 2008 and 2018, respectively.

He is the Professur Leistungselektronik with Elektrotechnisches Institut, TU Dresden. His research interests include modulation and control of power electronic converters, sliding mode, and flatness-based methods.